2D photochemical modeling of Saturn's stratosphere
Part I: Seasonal variation of atmospheric composition without meridional transport

V. Hue[a,b,*], T. Cavalié[c], M. Dobrijevic[a,b], F. Hersant[a,b], T. K. Greathouse[d]

[a]*Université de Bordeaux, Laboratoire d'Astrophysique de Bordeaux, UMR 5804, F-33270 Floirac, France*
[b]*CNRS, Laboratoire d'Astrophysique de Bordeaux, UMR 5804, F-33270, Floirac, France*
[c]*Max-Planck-Institut für Sonnensystemforschung, 37077, Göttingen, Germany*
[d]*Southwest Research Institute, San Antonio, TX 78228, United States*

Abstract

Saturn's axial tilt of 26.7° produces seasons in a similar way as on Earth. Both the stratospheric temperature and composition are affected by this latitudinally varying insolation along Saturn's orbital path. A new time-dependent 2D photochemical model is presented to study the seasonal evolution of Saturn's stratospheric composition. This study focuses on the impact of the seasonally variable thermal field on the main stratospheric C2-hydrocarbon chemistry (C_2H_2 and C_2H_6) using a realistic radiative climate model. Meridional mixing and advective processes are implemented in the model but turned off in the present study for the sake of simplicity. The results are compared to a simple study case where a latitudinally and temporally steady thermal field is assumed. Our simulations suggest that, when the seasonally variable thermal field is accounted for, the downward diffusion of the seasonally produced hydrocarbons is faster due to the seasonal compression of the atmospheric column during winter. This effect increases with increasing latitudes which experience the most important thermal changes in the course of the seasons. The seasonal variability of C_2H_2 and C_2H_6 therefore persists at higher-pressure levels with a seasonally-variable thermal field. Cassini limb-observations of C_2H_2 and C_2H_6 (Guerlet et al., 2009) are reasonably well-reproduced from the equator to 40° in both hemispheres

[*]Tel: +33-5-5777-**6164**

Email address: Vincent.Hue@obs.u-bordeaux1.fr (V. Hue)

in the 0.1-1 mbar pressure range. At lower pressure levels, the models only fit the Cassini observations in the northern hemisphere, from the equator to 40°N. Beyond 40° in both hemispheres, deviations from the pure photochemical predictions, mostly in the southern hemisphere, suggest the presence of large-scale stratospheric dynamics.

1. Introduction

Observations of Saturn in the infrared and millimetric range, performed by ISO or ground-based facilities gave us access to its disk-averaged stratospheric composition (see the review of Fouchet et al. (2009) for a complete list of observations), for which 1D photochemical models have done a fairly good job reproducing it (Moses et al., 2000a,b). Close-up observations, performed by the Voyager missions as well as recent ground-based observations, have unveiled variations with latitude of the temperature and the stratospheric composition (Ollivier et al., 2000a; Greathouse et al., 2005; Sinclair et al., 2014). The Cassini probe has now mapped (as a function of altitude and latitude) and monitored for almost 10 years, i.e. 1.5 Saturn season, the temperature and the main hydrocarbon emissions in Saturn's stratosphere (Howett et al., 2007; Fouchet et al., 2008; Hesman et al., 2009; Guerlet et al., 2009, 2010; Li et al., 2010; Fletcher et al., 2010; Sinclair et al., 2013, 2014).

We now have an impressive amount of data for which 1D photochemical models (e.g., Moses et al. 2000a,b, 2005 and Ollivier et al. 2000b) have become insufficient in predicting the 3D properties of Saturn's stratosphere, especially in terms of dynamics (diffusion and advection). On the other hand, general circulation models (GCM) are being developed for Jupiter (Medvedev et al., 2013) and Saturn (Dowling et al., 2006, 2010; Friedson and Moses, 2012; Guerlet et al., 2014). Such models usually focus on dynamics and therefore are restricted in their description of the atmospheric chemistry as they are limited to only a few reactions, if any at all.

Liang et al. (2005) and Moses and Greathouse (2005) made the first attempts to construct latitude-altitude photochemical models for the giant planets, followed by Moses et al. (2007) who built a 2D-photochemical model for Saturn and who accounted for simple Hadley-type circulation cells as well as meridional diffusive transport. The quasi-two-dimensional model developed by Liang et al. (2005) does not fully account for the latitudinal transport

2

as a diffusive correction is added at the end of the one-dimensional calculations. This model also does not account for evolution of the orbital parameters. Due to its very low obliquity, the seasonal effects on Jupiter should be mainly caused by its eccentricity and might be non negligible. On the other hand, the model developed by Moses and Greathouse (2005) accounts for the seasonal evolution of the orbital parameters as well as the variations in solar conditions. They have shown that, for Saturn, the seasonal effects on atmospheric composition are important, as Saturn's obliquity is slightly larger than the Earth's. Their model consists of a sum of 1D-photochemical model runs at different solar declinations and conditions. It does not include meridional transport processes nor the calculation of the actinic fluxes in 2D/3D. Saturn's high obliquity similarly impacts the stratospheric temperatures (Fletcher et al., 2010). This effect was accounted for by Moses and Greathouse (2005) in their photochemical model as part of a sensitivity case study, by locally warming their nominal temperature profile at two latitudes, according to the observations of Greathouse et al. (2005). In this sense, the photochemical model in Guerlet et al. (2010) represents an improvement from the previous model of Moses and Greathouse (2005) as it includes the latitudinal thermal gradient observed both by Fletcher et al. (2007) and Guerlet et al. (2009), but held constant with seasons. Finally, Moses et al. (2007) accounted for the meridional transport in a 2D-photochemical model, but similarly neglected the seasonal evolution of the stratospheric temperature. They were unable to reproduce the ground-based hydrocarbon observations prior to Cassini mission (Greathouse et al., 2005). After 10 years of Cassini measurements, data has shown that Saturn's stratospheric thermal structure is complex, with a 40K pole-to-pole gradient after solstice (Fletcher et al., 2010), and thermal oscillations in the equatorial zone (Orton et al., 2008; Fouchet et al., 2008; Guerlet et al., 2011).

For the moment, there is no 2D photochemical model that simultaneously accounts for seasonal forcing, meridional transport and the evolution of the stratospheric temperature. In this paper, we present a new step toward this model, applied to Saturn. These latitudinally and seasonally variable 1D models, coupled by a 3D-radiative transfer model, can be seen as an intermediate class of model between the 1D photochemical models that have the most complete chemistries and the GCMs that are focused on 3D dynamics. In this paper, we present a restricted version of our full-2D model. The goal of this preliminary study is to evaluate the atmospheric chemical response to seasonal forcing in terms of solar radiation and atmospheric temperatures.

3

The meridional transport is therefore set to zero for this study in order to focus on photochemical effects. In forthcoming papers we will focus on the effect of 2D advective and diffusive transport on the predicted abundances.

In the first part of this paper, we present in detail how the seasonally variable parameters are accounted for in the model, including Saturn's orbital parameters and the thermal field. Then, we describe the photochemical model, the chemical scheme used in that model and the 3D radiative transfer model used to calculate the attenuation of the UV radiation in the atmosphere. We afterwards describe the seasonal evolution of the chemical composition, first by assuming that the thermal field does not evolve with time and latitude, to compare with previous findings, then by considering a more realistic thermal field with spatio-temporal variations. We underline the effect of such thermal field variations on the chemical composition. Finally, we will compare our results with the Cassini/CIRS observations.

2. Seasonal modeling of the photochemistry

2.1. Introduction

The amount of solar radiation striking the top of the atmosphere at a given latitude varies with seasons because of Saturn's obliquity and eccentricity. Atmospheric heating occurs through methane near-IR absorption of this radiation. Cooling is preponderant in the mid-IR range, mainly through emissions from acetylene, ethane, and, to a lesser extent, methane (Yelle et al., 2001). These IR-emissions increase with increasing atmospheric temperatures and/or abundances of these compounds. Therefore, the temperature field, as a function of altitude and latitude, mostly depends on the seasonal distribution of these species and on their response to the seasonally varying insolation.

Methane, which is generally assumed to be well-mixed in Saturn's atmosphere (see e.g., Fletcher et al. 2009) and optically thick in its IR bands, can be used as a thermometer to constrain the thermal field (Greathouse et al., 2005). Asymmetries in Saturn's atmospheric temperatures have been observed as a function of season, from Voyager (Pirraglia et al., 1981; Hanel et al., 1981, 1982; Conrath and Pirraglia, 1983; Courtin et al., 1984) and ground-based observations (e.g., Gillett and Orton 1975; Rieke 1975; Tokunaga et al. 1978; Gezari et al. 1989; Ollivier et al. 2000a; Greathouse et al. 2005). These observations have been reproduced in an approximate sense by

radiative transfer model predictions (Cess and Caldwell, 1979; Bézard et al., 1984; Bézard and Gautier, 1985).

The Cassini spacecraft arrived in Saturn's system in July 2004, shortly after its northern winter solstice (see Fig. 1). It has provided full-coverage of the temperatures for the upper troposphere and stratosphere ever since. It has given us the opportunity to observe seasonal changes in the temperature field for over 10 years. For instance, the North/South thermal asymmetry at the northern winter solstice has been observed: the southern hemisphere was experiencing summer and was found warmer than the northern one (Flasar et al., 2005; Howett et al., 2007; Fletcher et al., 2007). Subsequently, Cassini observed how the winter hemisphere evolves when emerging from the shadow of the rings and how the summer hemisphere cools down when approaching equinox (Fletcher et al., 2010; Sinclair et al., 2013).

The main driver for atmospheric chemistry comes from solar UV radiation. This radiation initiates a complex chemistry through methane photolysis leading to the production of highly reactive chemical radicals. The kinetics of the chemical reactions triggered by photolysis generally have a thermal dependence that can impact the overall production/loss rates of atmospheric constituents over the course of Saturn's long seasons.

Since we want to evaluate the atmospheric chemical response to seasonal forcing in terms of solar radiation and atmospheric temperatures, we thus compare the results of our model obtained in two different cases:

- The temperature field consists of a single profile applied to all latitudes and seasons in a similar way to previous 1D studies. This study case will be denoted (U)

- The temperature field is vertically, latitudinally and seasonally variable. This study case will be denoted (S)

We stress again that the latitudes are not connected in the following study, i.e., the meridional transport is set to zero, so as to better quantify the effects of a seasonally variable temperature field on the distribution of chemical species. We defer the study of meridional transport to a forthcoming paper.

2.2. Accounting for Saturn's eccentric orbit

Due to Kepler's second law, Saturn's southern summer is shorter and hotter than the northern one, as Saturn reaches its perihelion shortly after the southern summer solstice (see Fig. 2). In the present model, Saturn's

elliptic orbit is sampled using a regularly spaced heliocentric longitude grid of 10°. From one orbital point to the next one, the integration time of the photochemical model is computed from the Kepler equation and Saturn's true anomaly. The true anomaly and heliocentric longitude are similar quantities, only differing by their relative origin, the former one being Saturn's perihelion whereas the latter being the Vernal equinox. The offset position in heliocentric longitude of Saturn's perihelion was set at 280.077° (Guerlet et al., 2014), a value based on J2000 parameters. Similarly to Moses and Greathouse (2005), integration over several orbits was needed for the simulations to converge down to the 100 mbar pressure level. Although the eddy diffusion coefficient profile as a function pressure was identical in every simulation, differences were found in the number of orbits required for convergence in the simulations depending on the thermal field. We will explain the reasons for these differences in section 4.2.
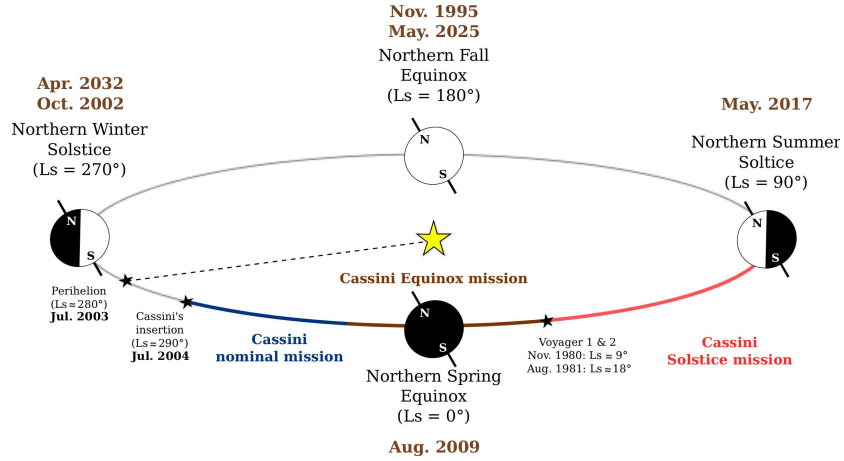

Figure 1: Overview of Saturn's seasons. The position of Saturn on its orbit is defined by its heliocentric longitude (L_s). $L_s = 0°$, $L_s = 90°$, $L_s = 180°$ and $L_s = 270°$ correspond to Saturn's northern vernal equinox, summer solstice, autumnal equinox and winter solstice, respectively. The Cassini orbital insertion around Saturn occurred on July 1, 2004, shortly after the northern winter solstice (Oct. 2002) and Saturn's perihelion (Jul. 2003). Cassini's nominal, equinox and solstice missions are indicated. Voyager missions 1 and 2 flew by Saturn system on Nov. 12, 1980 and on Aug. 26, 1981, respectively, for their closest encounters.

The variation of the solar declination as a function of the orbital fraction, starting from vernal equinox, is displayed in Fig. 2. As Saturn's perihelion

occurs shortly after the southern summer solstice, the orbital fraction during which the subsolar point is on the northern hemisphere is longer than the opposite one. This is shown by the solid curve being shifted to the right, at orbital fraction of 0.5, with respect to the circular case (dotted line).
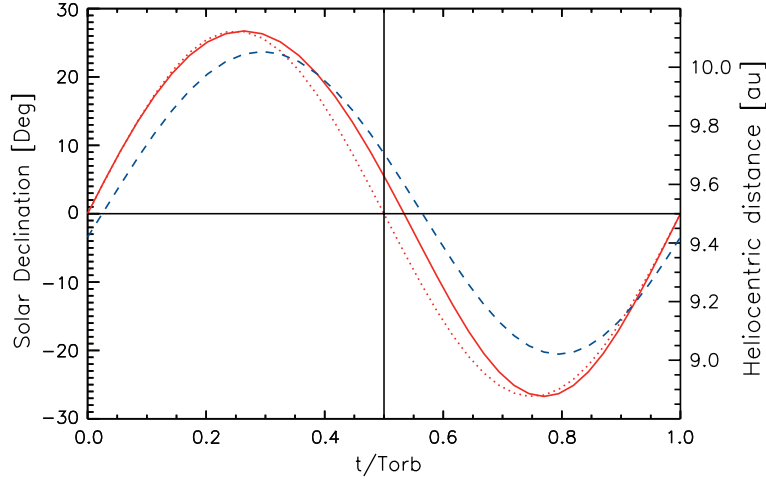

Figure 2: Variation of solar declination (left scale) as a function of the orbital fraction, assuming Saturn's eccentricity (red solid line) and null eccentricity (red dotted line). The origin of the orbital fraction is taken at the northern spring equinox. The corresponding variation of the heliocentric distance (dashed line, right scale) is also plotted. Saturn's perihelion occurs shortly after the northern winter solstice. The solid vertical line at t/T_{orb} $= 0.5$ denotes the moment when the planet has spent half of its orbital period. At this point the subsolar point is still on the northern hemisphere, due to Saturn eccentricity.

2.3. Temperature field

2.3.1. Spatially uniform thermal profile

In our first study case, the temperatures over the planet only vary with altitude and are constant with time and latitude, consistent with Moses and Greathouse (2005). We have taken the thermal profile that was used to obtain the reduced chemical scheme (Dobrijevic et al., 2011) we employ in our model. The temperatures below the 10^{-5} mbar pressure level come from a retrieval performed by Fouchet et al. (2008) on Cassini/CIRS data observed at a planetographic latitude of 20°S. Extrapolation to the upper stratosphere has been made using data from Smith et al. (1983) (see Fig. 4). This thermal profile is presented in Fig. 4. In what follows, we will refer to this case as the "spatially uniform" (U) temperature field case.

7

2.3.2. Seasonally variable thermal field

The second temperature field we considered comes from the seasonal radiative climate model of Greathouse et al. (2008), which has already been compared to Cassini/CIRS observations (Fletcher et al., 2010). This radiative transfer model takes into account heating and cooling from Saturn's major atmospheric compounds, i.e. CH_4, C_2H_2, and C_2H_6, as well as seasonal variation of Saturn's orbital parameters, i.e., solar declination, heliocentric distance and eccentricity. It also includes ring shadowing and accounts for Saturn's oblate shape. In this second study case, the temperature varies with altitude, latitude and time. This case will be referred to as the "seasonal" (S) temperature field case.

The seasonal thermal field used in this paper is shown in Fig. 3 as a function of planetocentric latitudes and heliocentric longitudes, and is presented for two pressure levels: 0.1 mbar and 10 mbar. Hereafter, all quoted latitudes are planetocentric, if not otherwise specified. The North-South asymmetry during the summer is caused by Saturn's eccentricity. The effects of ring shadowing are clearly observed at 0.1 mbar, around the solstices between 0° and 40° planetocentric latitude in the winter hemispheres. Time-lag between temperatures and seasons, due to the atmospheric thermal-inertia, can be seen at 10 mbar by the difference in temperature profile at 0.1 and 10 mbar. The thermal field has been computed by taking, as a first guess, the CH_4, C_2H_2 and C_2H_6 vertical distributions observed by Cassini (Guerlet et al., 2009) at planetographic latitude of 45°S and held fixed with time.

The temperature map predicted from the radiative climate model is calculated within the pressure range from 500 mbar to 10^{-6} mbar (Fletcher et al., 2010; Greathouse et al., 2008). Although the seasonal model of Greathouse et al. (2008) extends down to 500 mbar, temperatures are only accurate to 10 mbar as this model was created primarily to model the stratosphere. At lower altitudes, the model lacks aerosol absorption and scattering and convective adjustement. Due to this lack of aerosols, the tropospheric temperatures are lower by 5-15 K than measured by Cassini. We note this discrepancy, but are focused on understanding effect of temperature on stratospheric photochemistry occur at altitudes above the 10 mbar level where the physics are self consistent. Below the 500 mbar level we extrapolate the temperature assuming a dry adiabatic lapse rate, using a specific heat of $c_p = 10\ 658$ J.kg^{-1}.K^{-1} (Irwin, 2006) and a latitude-dependent gravity field (see Supplementary Materials of Guerlet et al. 2014). Above 10^{-6} mbar, where non-LTE
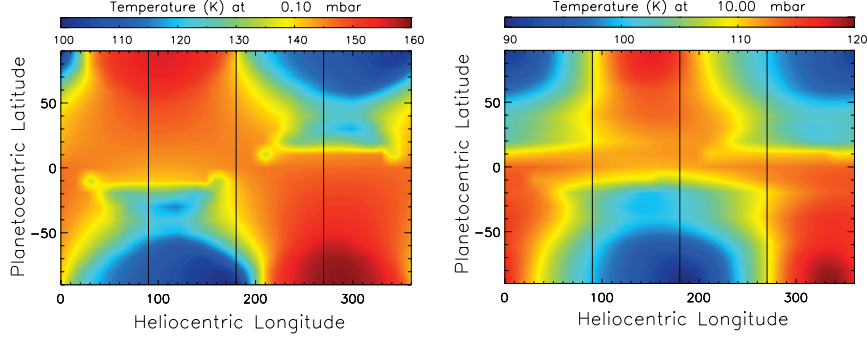
Figure 3: Seasonal temperature field inferred from the radiative climate model of Greathouse et al. (2008) as a function of planetocentric latitude and heliocentric longitude. The temperature variation at 0.1 mbar is twice as large as that at 10 mbar due to the increase in thermal inertia with depth in the atmosphere (note the color range is stretched differently for the two plots). Left panel: Temperatures at 0.1 mbar. Right panel: Temperatures at 10 mbar.

effects dominate, the temperature was held constant, and no thermosphere is assumed above the stratosphere in this model. The lowest pressure level in our grid is set in order to ensure that each monochromatic optical depth is smaller than 1 in the UV at the top of the atmosphere. Fig. 4 displays the resulting temperature profiles at 4 latitudes : 80°S (upper-left panel), 60°S (upper-right panel), 40°S (lower left panel) and the equator (lower right panel). The colored solid lines represent the atmospheric temperatures inferred from the radiative climate model at solstices and equinoxes and the reconstruction procedure described above.

2.3.3. Thermal evolution

The first case studied in this paper, namely the spatially uniform thermal field does not require special care on how the pressure-altitude background is treated, as it remains constant all along the year. However, when the temperature changes, i.e., in the case of a seasonally variable thermal field, the pressure-altitude background also changes and has to be handled carefully.

Two ways of dealing with changes in the atmospheric pressure-temperature background in photochemical modeling exist. Either the altitude grid is held constant and the pressure varies with temperature, or the pressure grid is held constant and the altitude grid is free to contract or expand (e.g., Agúndez et al. 2014). Since the two approaches are self-consistent, we have choosen
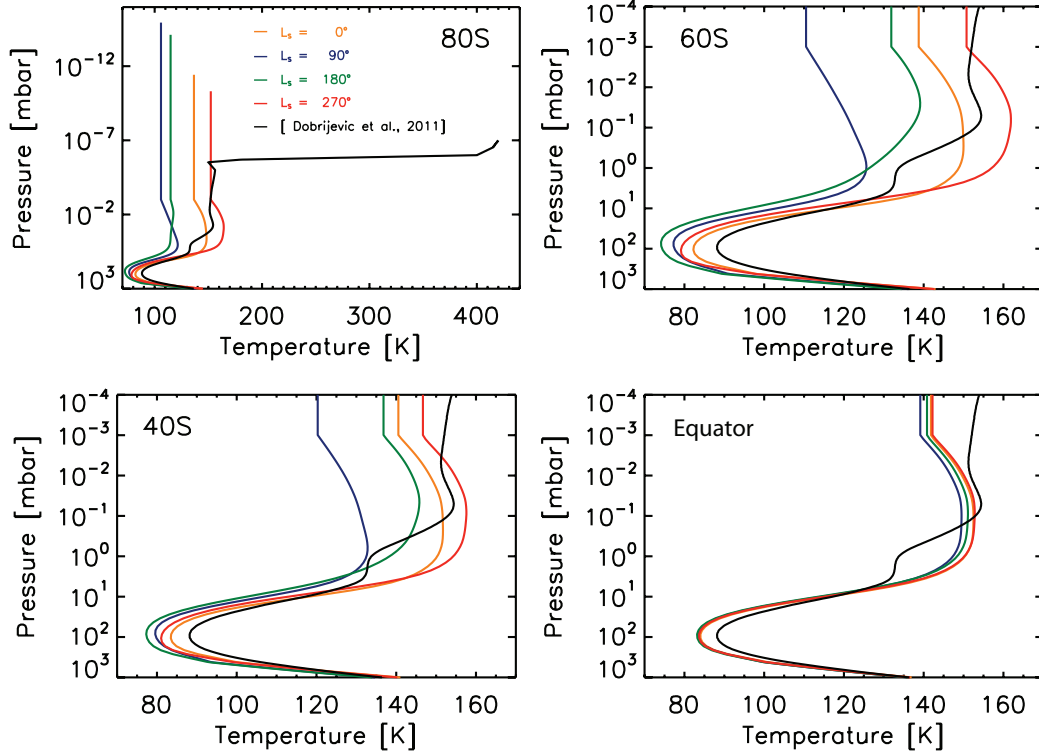
9

Figure 4: Temperature profiles used in this work as a function of pressure. The colored lines depict the seasonally variable thermal field (S) predicted from the radiative climate model at the solstices and equinoxes, for 4 latitudes : 80°S (upper-left panel), 60°S (upper-right panel), 40°S (lower left panel) and the equator (lower left panel). $L_s = 0°$, 90°, 180° and 270° correspond to northern fall equinox, summer solstice, spring equinox and winter solstice, respectively (see Fig. 1). The black solid lines display the spatially uniform thermal field (U) we consider in this work. This profile comes from Cassini/CIRS observations (Fouchet et al., 2008) and Voyager 2 observations (Smith et al., 1983) (see text for details).

to hold the altitude grid constant and let the pressure grid vary with temperature.

This choice has been made to allow two latitudinally-contiguous numerical cells to exchange material through their common boundary, for future 2D-modeling including circulation and meridional advection.

The altitude-temperature grid at all latitudes and heliocentric longitudes is built assuming hydrostatic equilibrium. Variations in scale height due to Saturn's latitudinally and altitudinally-dependent gravity field and variations in the mean molecular mass in the upper atmosphere due to molecular diffusion are included when solving the hydrostatic equilibrium equation. The latitudinal-dependency adopted here follows the prescription of Guerlet et al. (2014). We have made sure that the pressure-temperature background using this prescription is consistent with the latitudinally dependent gravitational field published by Lindal et al. (1985) and combined with the Voyager 2 zonal wind measurements (Smith et al., 1982; Ingersoll and Pollard, 1982).

The effect on the pressure-altitude grid can be large as shown in Fig. 5, which presents this grid for 80°N at the equinoxes and solstices. Solid and dashed lines respectively represent this grid when the latitudinally-dependent gravity is included and when considering a constant surface gravity, set to the equatorial one. The pressure-altitude grid of the uniform model (see 2.3.1) is also shown (black solid line) for comparison. Differential surface gravity due to Saturn's high rotation rate results in more contracted atmospheric columns at polar latitudes. Hence, at the same altitude level, the pressure is lower at the poles relative to the equator when considering variable surface gravity. At a given latitude, the column also expands or contracts with temperature as shown in Fig. 5. This example at 80° N is extreme as the amplitude of the temperature variation with season is maximum at polar latitudes. The seasonal variation of the pressure-altitude grid is damped toward the equator, as the seasonal thermal gradient is reduced in this region.

In the present paper, we have chosen to work with a common altitude grid for all latitudes and seasons that start at a common origin ($z = 0\,\mathrm{km}$ and $P = 1\,\mathrm{bar}$). Above that origin, the pressure grid expands or contracts according to temperature changes. The mole fraction vertical profiles of the model species are expressed as a function of pressure and thus follow the same contraction/expansion as the pressure grid. Therefore, each time the temperature/pressure grid changes, the mole fraction profiles are interpolated onto the new pressure grid.

It is instructive to represent the seasonal evolution of the temperature
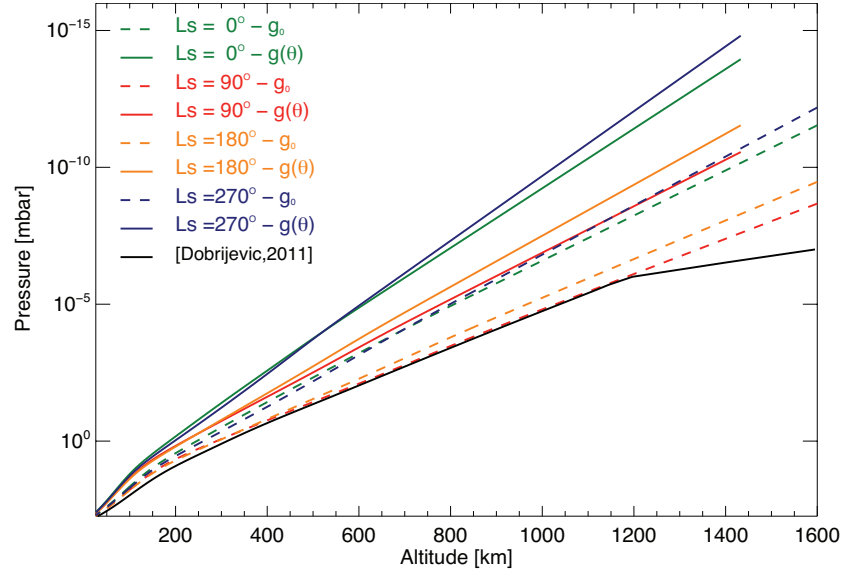
Figure 5: Pressure-altitude grid at 80°N for the solstices and equinoxes, assuming a constant surface gravity (dashed colored lines) and a latitudinally-variable surface gravity (solid colored lines). $L_s = 0°$, 90°, 180° and 270° correspond to northern fall equinox, summer solstice, spring equinox and winter solstice, respectively (see Fig. 1). 0 km is equal to the 1 bar level. The black solid line represents the pressure-altitude grid of the uniform temperature profile.

and pressure at a given latitude for a few altitude levels (see Fig. 6 for an illustration at 80°N). When the temperature rises, the atmospheric column expands, and the associated pressure at the same altitude increases. It should be noted that temperature and pressure are not totally in phase, as the pressure at a given altitude depends on the thermodynamical conditions of the altitude levels underneath. Therefore the temperature at a few altitude levels below the considered altitude are presented on the same figure. We note that the increase in the pressure at 300 km is in phase with the temperature changes at altitude levels below that level.
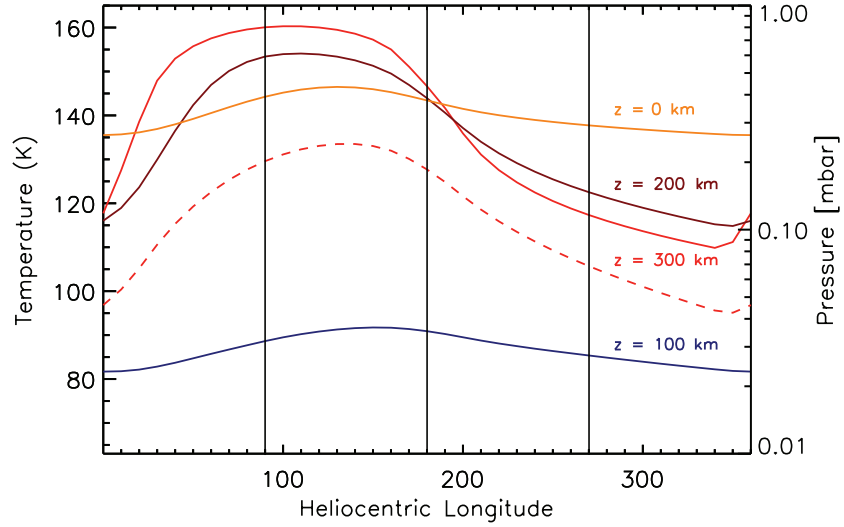

Figure 6: Seasonal evolution of temperature (left scale, solid lines) and pressure (right scale, dashed line) at altitudes of 300 km (red lines), 200 km (brown), 100 km (blue) and 0 km (orange). The quantities are presented for a planetocentric latitude of 80°N, where the variations are most noticeable. The black solid lines indicate the position of the solstices and equinoxes (see Fig. 1).

3. Latitudinally and seasonally variable 1D models

3.1. General description

In an atmosphere, the spatio-temporal distribution of each species' number density is governed by the continuity-transport equation, that is:

$$\frac{\partial n_i}{\partial t} = P_i - n_i L_i - \nabla \cdot (\mathbf{\Phi_i}) \tag{1}$$

13

where n_i [cm^{-3}] is the number density, P_i [cm^{-3} s^{-1}] the (photo)chemical production rate, L_i [s^{-1}] the (photo)chemical loss rate and Φ_i [cm^{-2} s^{-1}] is the particle flux due to transport. Longitudinal mixing timescales appear to be relatively short in Jupiter's atmosphere (*e.g.,* Banfield et al. 1996) and deviations from the mean zonal temperatures are limited (Flasar et al., 2004). We assume the situation is similar at Saturn and we thus do not consider longitudinal variability in this study. The continuity equation is then solved on a 2D altitude-latitude spherical grid. We use a 13 km altitude grid resolution, in order to have at least 3 altitudinal numerical cells per scale height at all times throughout the year. The planet radius considered here is Saturn's mean radius, $R = 58,210$ km (Guillot, 2005), which corresponds to the altitude level $z = 0$ km. The flux Φ_i includes transport processes in the vertical and the meridional directions.

Taking these mixing processes into account at all scales and in detail would require a full hydrodynamical model, which is beyond the scope of this work. In our model, the physical processes that are accounted for through the vertical flux Φ_i^z, are eddy diffusion, molecular diffusion and vertical advection. This flux is expressed as:

$$\Phi_i^z = -\, D_i n_i \left(\frac{1}{y_i} \frac{\partial y_i}{\partial z} + \frac{1}{H_i} - \frac{1}{H} \right) - K_{zz} n_i \left(\frac{1}{y_i} \frac{\partial y_i}{\partial z} \right) + v_i^z n_i \qquad (2)$$

where y_i is the mole fraction of species i, defined as the ratio between the number density of i over the total number density. H_i and H [cm] are respectively the specific and the mean density scale height, D_i [cm^2 s^{-1}] the molecular diffusion coefficient, K_{zz} [cm^2 s^{-1}] the vertical eddy diffusion coefficient and v_i^z [cm s^{-1}] the vertical wind. The numerical scheme used in this study is similar to the one used by Agúndez et al. (2014) in their pseudo-2D photochemical model except that we use an upwind scheme to treat the advective part of the molecular diffusion (Godunov, 1959). The meridional flux Φ_i^θ is set to zero for the current study.

The vertical eddy diffusion coefficient K_{zz} is a free parameter in the model to account for mixing processes caused by dynamics occuring at every scale. This parameter may vary with altitude and latitude, but our knowledge for giant planet stratospheres is very limited (see for instance Moreno et al. 2003 and Liang et al. 2005). This coefficient is related to the small-scale waves and is therefore expected to be influenced by the atmospheric number

density (Lindzen, 1971, 1981). Consequently, 2D/3D models will probably have to account for its latitudinal and longitudinal variability. In this study, we consider that K_{zz} is fixed with respect to the pressure coordinate. Due to the lack of constraint on that parameter, we consider this does not vary with latitude. The reduced chemical scheme we use has been obtained using the K_{zz} profile of Dobrijevic et al. (2011). Therefore, we consistently take their K_{zz}. The molecular diffusion coefficient we adopt is based on experimental measurements of binary gas diffusion coefficients (Fuller et al., 1966, 1969). As a first step in this study, we set K_{yy}, v^z and v^θ to zero. These parameters will be studied in a forthcoming paper, either by trying to fit them from the observations or by testing outputs of the yet-to-be-finalized GCM of Guerlet et al. (2014).

At the lower boundary of the model (i.e. 1 bar), the H_2 and He mole fractions are set to 0.8773 and 0.118, respectively (Conrath and Gautier, 2000). The methane mole fraction was set to 4.7×10^{-3} according to recent Cassini/CIRS observations (Fletcher et al., 2009). At this boundary, all other compounds diffuse down to the lower troposphere at their maximum diffusion velocity, i.e., $v = -K_{zz}(0)/H(0)$. At the upper boundary of the model, all fluxes are set to zero except for atomic hydrogen. Following Moses et al. (2005), we set its influx to $\Phi_H = 1.0 \times 10^8 \mathrm{~cm}^{-2}\mathrm{~s}^{-1}$ at all latitudes.

3.2. Chemical Scheme

In typical 1D photochemical models, the chemical schemes contain as many reactions as possible, i.e., usually hundreds, and numerous species. This makes it extremely difficult for current computers to solve equation (1) in a reasonable time when extending such models to 2D or 3D. Dobrijevic et al. (2011) have developed an objective methodology to reproduce the chemical processes for a subset of compounds of interest (usually observed compounds) with a limited number of reactions. These are extracted from a more complete chemical scheme by running a 1D photochemical model and applying propagation of uncertainties on chemical rates and a global sensitivity analysis.

Uncertainties in the chemical rate constants are a critical source of uncertainty in photochemical model predictions (Dobrijevic and Parisot, 1998), as chemical schemes generally include tens to hundreds of chemical compounds, non-linearly coupled in even more reactions. Propagating uncertainties on each chemical reaction, using a Monte Carlo procedure for instance, can lead to several orders of magnitude in uncertainty (Dobrijevic et al., 2003). By

15

computing correlations between reaction rate uncertainties and photochemical model predictions, Dobrijevic et al. (2010a) and Dobrijevic et al. (2010b) developed a global sensitivity analysis methodology to identify key reactions in chemical schemes. These reactions have a major impact on the results, either because their uncertainty is intrinsically high, or because they significantly contribute in the production/loss terms of the compound of interest (or one of the compounds related to it).

A reaction that has a low degree of significance means that changing its rate constant (within its uncertainty range) does not significantly change the results of the model, or well inside the model error bars. Building a reduced network then consists in removing reactions, and thus compounds once they are no longer linked by reactions, that have a very low degree of significance. The results stay very close to the median profile of the full chemical scheme for the remaining compounds.

A reduced chemical scheme is valid when it agrees with the full chemical scheme, given the uncertainties of each chemical compound profile. The initial scheme we consider includes 124 compounds, 1141 reactions and 172 photodissociation processes and comes from Loison et al. (2014). The compounds we have selected to build the reduced chemical scheme are the ones monitored by Cassini/CIRS and most relevant regarding stratospheric heating and cooling: CH_4, C_2H_2, and C_2H_6 (Guerlet et al., 2009; Sinclair et al., 2013). We based our reduction scheme on the model validation performed for Saturn's hydrocarbons by Cavalié et al. 2015. C_2H_2, and C_2H_6 vertical profiles using the reduced chemical scheme are in good agreement with the full chemical scheme results (Fig. 7). The reduced scheme produces vertical profiles that are within the 5th and 15th of the full-scheme 20-quantiles distribution for C_2H_6 at all pressure levels and for C_2H_2 above 10 mbar. Below 10 mbar, the C_2H_2 vertical profile is almost superimposed to the 15th 20-quantiles of the distribution.

Three main oxygen compounds have also been added to the reduced scheme which are present in Saturn's stratosphere (H_2O, CO, and CO_2) as ground work for a forthcoming paper on the spatial distribution of H_2O, following observations by Herschel (Hartogh et al., 2009, 2011). The oxygen species will not be used in the present study and will not be presented nor discussed any further. In the end, the reduced scheme used in the present study includes 22 compounds, 33 reactions, and 24 photodissociations, listed in Table 1. Such a reduced chemical scheme enables extending photochemical computations to 2D/3D.
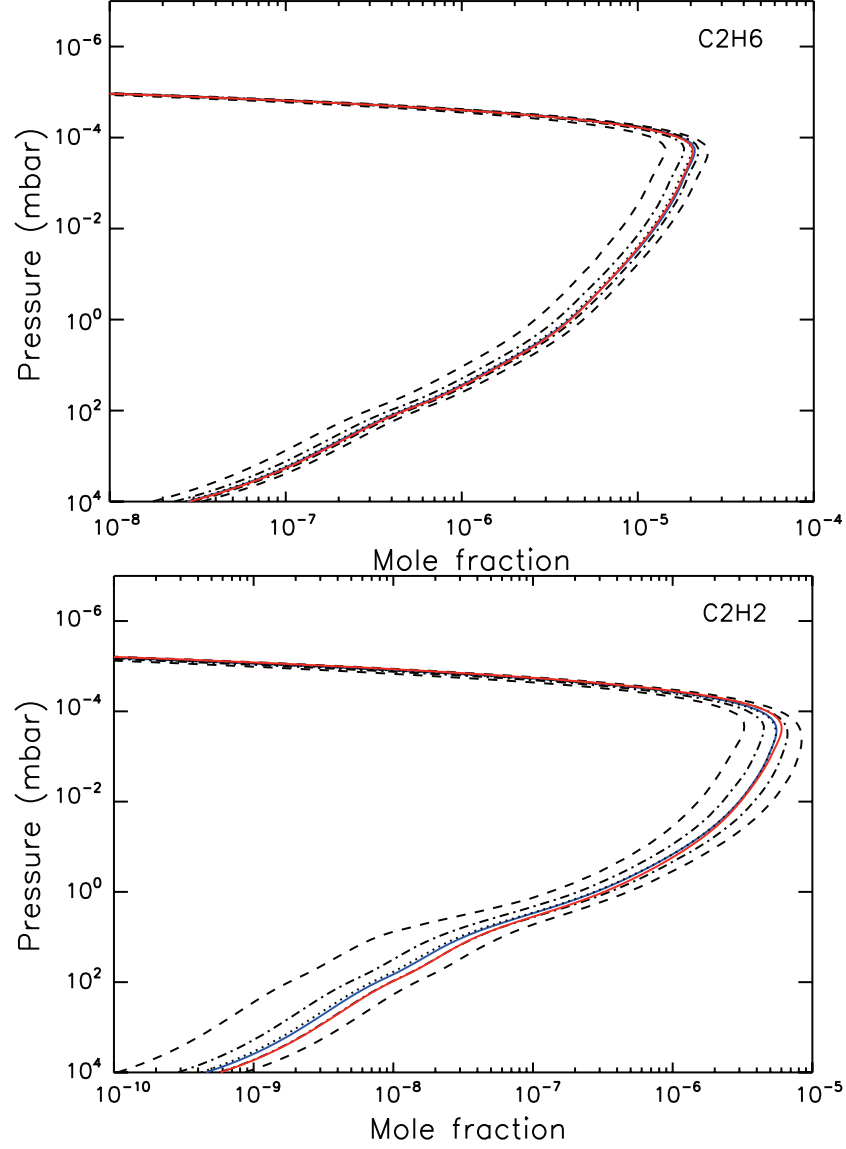
16

Figure 7: Red solid line: C_2H_6 (top panel) and C_2H_2 (botom panel) vertical profile with the reduced chemical scheme. Blue line: nominal vertical profile obtained using the initial chemical scheme. Black dotted line: median profile of the full-scheme distribution. Black dashed-dotted lines: 5th and 15th 20-quantiles of the full-scheme distribution. Black dashed lines: 1th and 19th 20-quantiles of the full-scheme distribution.

Table 1: List of the 22 chemical compounds included in the scheme

He; H; H_2
CH; C; $^1CH_2$; $^3CH_2$; CH_3; CH_4
C_2H; C_2H_2; C_2H_3; C_2H_4; C_2H_5; C_2H_6
O^3P; O^1D; OH; H_2O
CO; CO_2; H_2CO

Table 2: List of reactions of the reduced network (references can be found in Loison et al. (2014)). $k(T) = \alpha \times (T/300)^{\beta} \times \exp(-\gamma/T)$ in cm^3 molecule^{-1} s^{-1} or cm^6 molecule^{-1} s^{-1}. $k_{adduct} = (k_0 \, [M] \, F + k_r) \, k_{\infty}/k_0[M] + k_{\infty}$ with $\log(F) = \log(F_c)/1 + [\log(k_0[M] + k_{capture})/N]^2$, $F_c = 0.60$ and $N = 1$. Please refer to Hébrard et al. (2013) for details about the semi-empirical model.

	Reactions		Rate coefficients
R1	H + CH	$\rightarrow$ C + H_2	$1.24 \times 10^{-10} \times (T/300)^{0.26}$
R2	H + $^3CH_2$	$\rightarrow$ CH + H_2	$2.2 \times 10^{-10} \times (T/300)^{0.32}$
R3	H + $^3CH_2$	$\rightarrow CH_3$	$k_0 = 3.1 \times 10^{-30} \times \exp(457/T)$
			$k_{\infty} = 1.5 \times 10^{-10}$
			$k_r = 0$
R4	H + CH_3	$\rightarrow CH_4$	$k_0 = 8.9 \times 10^{-29} \times (T/300)^{-1.8} \times \exp(-31.8/T)$
			$k_{\infty} = 3.2 \times 10^{-10} \times (T/300)^{0.133} \times \exp(-2.54/T)$
			$k_r = 1.31 \times 10^{-16} \times (T/300)^{-1.29} \times \exp(19.6/T)$
R5	H + C_2H_2	$\rightarrow C_2H_3$	$k_0 = 2.0 \times 10^{-30} \times (T/300)^{-1.07} \times \exp(-83.8/T)$
			$k_{\infty} = 1.17 \times 10^{-13} \times (T/300)^{8.41} \times \exp(-359/T)$
			$k_r = 0$
R6	H + C_2H_3	$\rightarrow C_2H_2 + H_2$	6.0×10^{-11}
R7	H + C_2H_3	$\rightarrow C_2H_4$	$k_0 = 3.47 \times 10^{-27} \times (T/300)^{-1.3}$
			$k_{\infty} = 1.0 \times 10^{-10}$
			$k_r = 0$
R8	H + C_2H_4	$\rightarrow C_2H_5$	$k_0 = 1.0 \times 10^{-29} \times (T/300)^{-1.51} \times \exp(-72.9/T)$
			$k_{\infty} = 6.07 \times 10^{-13} \times (T/300)^{-5.31} \times \exp(174/T)$
			$k_r = 0$
R9	H + C_2H_5	$\rightarrow C_2H_6$	$k_0 = 2.0 \times 10^{-28} \times (T/300)^{-1.5}$
			$k_{\infty} = 1.07 \times 10^{-10}$
			$k_r = 0$
R10	H + C_2H_5	$\rightarrow CH_3 + CH_3$	$k_0 = k_{\infty} - k_{adduct}$

R11	$C + H_2$	$\rightarrow {}^3CH_2$	$k_0 = 7.0 \times 10^{-32} \times (T/300)^{-1.5}$
			$k_\infty = 2.06 \times 10^{-11} \times \exp(-57/T)$
			$k_r = 0$
R12	$CH + H_2$	$\rightarrow CH_3$	$k_0 = 6.2 \times 10^{-30} \times (T/300)^{-1.6}$
			$k_\infty = 1.6 \times 10^{-10} \times (T/300)^{-0.08}$
			$k_r = 0$
R13	$CH + CH_4$	$\rightarrow C_2H_4 + H$	$1.05 \times 10^{-10} \times (T/300)^{-1.04} \times \exp(-36.1/T)$
R14	${}^1CH_2 + H_2$	$\rightarrow {}^3CH_2 + H_2$	$1.6 \times 10^{-11} \times (T/300)^{-0.9}$
R15	${}^1CH_2 + H_2$	$\rightarrow CH_3 + H$	$8.8 \times 10^{-11} \times (T/300)^{0.35}$
R16	${}^3CH_2 + H_2$	$\rightarrow CH_3 + H$	$8.0 \times 10^{-12} \times \exp(-4500/T)$
R17	${}^3CH_2 + CH_3$	$\rightarrow C_2H_4 + H$	1.0×10^{-10}
R18	${}^3CH_2 + C_2H_3$	$\rightarrow C_2H_2 + CH_3$	3.0×10^{-11}
R19	${}^3CH_2 + C_2H_5$	$\rightarrow C_2H_4 + CH_3$	3.0×10^{-11}
R20	$CH_3 + CH_3$	$\rightarrow C_2H_6$	$k_0 = 1.8 \times 10^{-26} \times (T/300)^{-3.77} \times \exp(-61.6/T)$
			$k_\infty = 6.8 \times 10^{-11} \times (T/300)^{-0.359} \times \exp(-30.2/T)$
			$k_r = 0$
R21	$C_2H + H_2$	$\rightarrow C_2H_2 + H$	$1.2 \times 10^{-11} \times \exp(-998/T)$
R22	$C_2H + CH_4$	$\rightarrow C_2H_2 + CH_3$	$1.2 \times 10^{-11} \times \exp(-491/T)$
R23	$C_2H_3 + H_2$	$\rightarrow C_2H_4 + H$	$3.45 \times 10^{-14} \times (T/300)^{2.56} \times \exp(-2530/T)$
R24	$C_2H_3 + CH_4$	$\rightarrow C_2H_4 + CH_3$	$2.13 \times 10^{-14} \times (T/300)^{4.02} \times \exp(-2750/T)$
R25	$O({}^3P) + CH_3$	$\rightarrow CO + H_2 + H$	2.9×10^{-11}
R26	$O({}^3P) + CH_3$	$\rightarrow H_2CO + H$	1.1×10^{-10}
R27	$O({}^3P) + C_2H_5$	$\rightarrow OH + C_2H_4$	3.0×10^{-11}
R28	$O({}^1D) + H_2$	$\rightarrow OH + H$	1.1×10^{-10}
R29	$OH + H_2$	$\rightarrow H_2O + H$	$2.8 \times 10^{-12} \times \exp(-1800/T)$
R30	$OH + CH_3$	$\rightarrow H_2O + {}^1CH_2$	3.2×10^{-11}
R31	$OH + CH_3$	$\rightarrow H_2CO + H_2$	8.0×10^{-12}
R32	$OH + CO$	$\rightarrow CO_2 + H$	1.3×10^{-13}
R33	$H_2CO + C$	$\rightarrow CO + {}^3CH_2$	4.0×10^{-10}

3.3. Actinic Flux

The knowledge of the solar UV flux at any latitude/altitude/season is required to properly compute photodissociation coefficients. We use a full-3D spherical line-by-line radiative transfer model, improved over the model initially developed by Brillet et al. (1996), to account for the attenuation of

Table 3: Photodissocation processes (References can be found in Loison et al. 2014)

	Photodissociations	
R34	$OH + h\nu$	$\rightarrow O(^1D) + H$
R35	$H_2O + h\nu$	$\rightarrow H + OH$
R36		$\rightarrow H_2 + O(^1D)$
R37		$\rightarrow H + H + O(^3P)$
R38	$CO + h\nu$	$\rightarrow C + O(^3P)$
R39	$CO_2 + h\nu$	$\rightarrow C + O(^1D)$
R40		$\rightarrow CO + O(^3P)$
R41	$H_2 + h\nu$	$\rightarrow H + H$
R42	$CH_4 + h\nu$	$\rightarrow CH_3 + H$
R43		$\rightarrow {}^1CH_2 + H + H$
R44		$\rightarrow {}^1CH_2 + H2$
R45		$\rightarrow {}^3CH_2 + H + H$
R46		$\rightarrow CH + H_2 + H$
R47	$CH_3 + h\nu$	$\rightarrow {}^1CH_2 + H$
R48	$C_2H_2 + h\nu$	$\rightarrow C_2H + H$
R49	$C_2H_3 + h\nu$	$\rightarrow C_2H_2 + H$
R50	$C_2H_4 + h\nu$	$\rightarrow C_2H_2 + H_2$
R51		$\rightarrow C_2H_2 + H + H$
R52		$\rightarrow C_2H_3 + H$
R53	$C_2H_6 + h\nu$	$\rightarrow C_2H_4 + H_2$
R54		$\rightarrow C_2H_4 + H + H$
R55		$\rightarrow C_2H_2 + H_2 + H_2$
R56		$\rightarrow CH_4 + H_2 + H_2$
R57		$\rightarrow CH_3 + CH_3$

solar UV in the atmosphere. It now accounts for the full 3D distribution of absorbers instead of assuming vertically homogeneous distributions in latitude and longitude as in Brillet et al. (1996). However, as stated previously, we consider here a zonally mixed atmosphere and limit variability to altitude and latitude. Absorption is formally calculated by the exact computation of the optical path. Rayleigh diffusion is also accounted for using single photon ray tracing in a Monte Carlo procedure. The wavelengths considered here range from 10 nm to 250 nm, because the hydrocarbons considered in this

study do not substantially absorb beyond these limits. The radiative transfer procedure uses the altitude-latitude absorption and diffusion coefficients, extrapolated onto a 3D atmosphere assuming zonal homogeneity. Correspondence between subsolar and planetocentric coordinates is then made assuming Saturn's orbital parameters at the moment of the Kronian year, i.e., when the altitude-latitude-longitude actinic flux needs to be computed. Saturn's ellipsoidal shape is not taken into account, while the elliptical orbit is. The elliptical orbit causes a peak in actinic flux during southern summer.

The daily-averaged actinic flux $[\mathrm{W\,m^{-2}}]$ at the top of the atmosphere is shown in Fig. 8. Actinic flux, unlike solar insolation, does not refer to any specifically oriented collecting surface. This is a fundamental quantity for photochemistry, since we consider that molecules do not preferentially absorb radiation with respect to any particular orientation in space. This quantity is therefore not corrected by the cosine of the incident angle, unlike insolation. From this 3D actinic flux, the daily-averaged insolation is computed. As a comparison with Fig. 8, Fig. 9 presents the daily-averaged solar insolation $[\mathrm{W\,m^{-2}}]$ received by a horizontal unit surface in Saturn's atmosphere. Following Moses and Greathouse (2005), we use a solar constant of 14.97 $\mathrm{W\,m^{-2}}$ for these calculations. In both figures, the effect of Saturn's elliptical orbit is obvious. Since Saturn reaches its perihelion shortly after the summer solstice, the amount of solar flux is more important at this time. The dark blue areas in the winter hemispheres indicate polar nights.

Ring shadowing effects due to the A-B-C rings and to the Cassini division are also included. Brinkman and McGregor (1979) and Bézard (1986) have first calculated ring shadowing in atmospheric models, however we adopt the prescription of Guerlet et al. (2014), which is more suited for implementation in our photochemical model. This method calculates whether or not a point on the planet at a given latitude and longitude is under the shadow of the rings. If this is the case, the solar flux at this point is reduced by the ring opacity. We adopt the normal opacity profile of the rings from Guerlet et al. (2014), which is based on more than 100 stellar occultations measured by the UVIS instrument aboard Cassini (Colwell et al., 2010). Finally, these normal opacities are corrected to account for the incidence angle of radiation over the rings. Diffusion effects from the ring are not included. We account for the latitudinal extent of the numerical cells in our calculations. Here we present results from simulations that use 10°-wide latitudinal cells. Therefore, the ring occultation is averaged over these 10°-wide cells. Each of the 10°-wide cells have been sampled over 0.1°-wide sub-cell. The effect of ring shadowing

21

can be seen at mid latitudes in the winter hemispheres in Figs. 8 and 9.

4. Results

In this section, we first present results from our photochemical model using the spatially uniform thermal field (U) described in 2.3.1 in order to compare with existing models (Moses and Greathouse, 2005). We detail the variability in hydrocarbon abundances as a function of altitude/latitude/time only due to the variation of the heliocentric distance of Saturn and of the latitude of the sub-solar point. Then, we give a brief overview of the influence of the rings on chemistry. Finally, we present the effect induced by the seasonal temperature field (S) and compare the results with the spatially uniform case. The interest here lies in the fact that we first present photochemical results using a simple test-case, i.e. a spatio-temporally uniform case previously studied (Moses and Greathouse, 2005), before adding more complexity by considering a more realistic thermal field.

4.1. Seasonal variability with the spatially uniform thermal field

We present here the results from seasonal simulations using the spatially uniform (U) temperature field, with an emphasis on methane, ethane and acetylene as they are the most important compounds with respect to the radiative heating/cooling of the atmosphere (Yelle et al., 2001).

4.1.1. Methane (CH_4), ethane (C_2H_6) and acetylene (C_2H_2)

The vertical profiles of CH_4, C_2H_6, and C_2H_2, using the spatially uniform temperature field, are displayed in Fig. 10.

CH_4 does not exhibit strong seasonal variations, as eddy mixing and molecular diffusion, rather than photolysis, are the major processes controlling the shape of its vertical distribution (Romani and Atreya, 1988). Indeed, due to its relatively high abundance, CH_4 is never depleted enough to show seasonal variations.

The seasonal variability on C_2H_6 is clearly seen at low-pressure levels. The shape of its vertical profile is mostly governed by reaction R20 ($CH_3 + CH_3 \rightarrow C_2H_6$). Methyl is produced from the CH_4 photolysis around 10^{-4} mbar. At higher pressures, C_2H_6 is mostly in diffusive equilibrium (see Zhang et al. 2013 for instance) and its shape is governed by the slow diffusion of C_2H_6 produced at lower pressure levels. The seasonal variability of this compound is correlated with insolation and is therefore maximum around the poles.
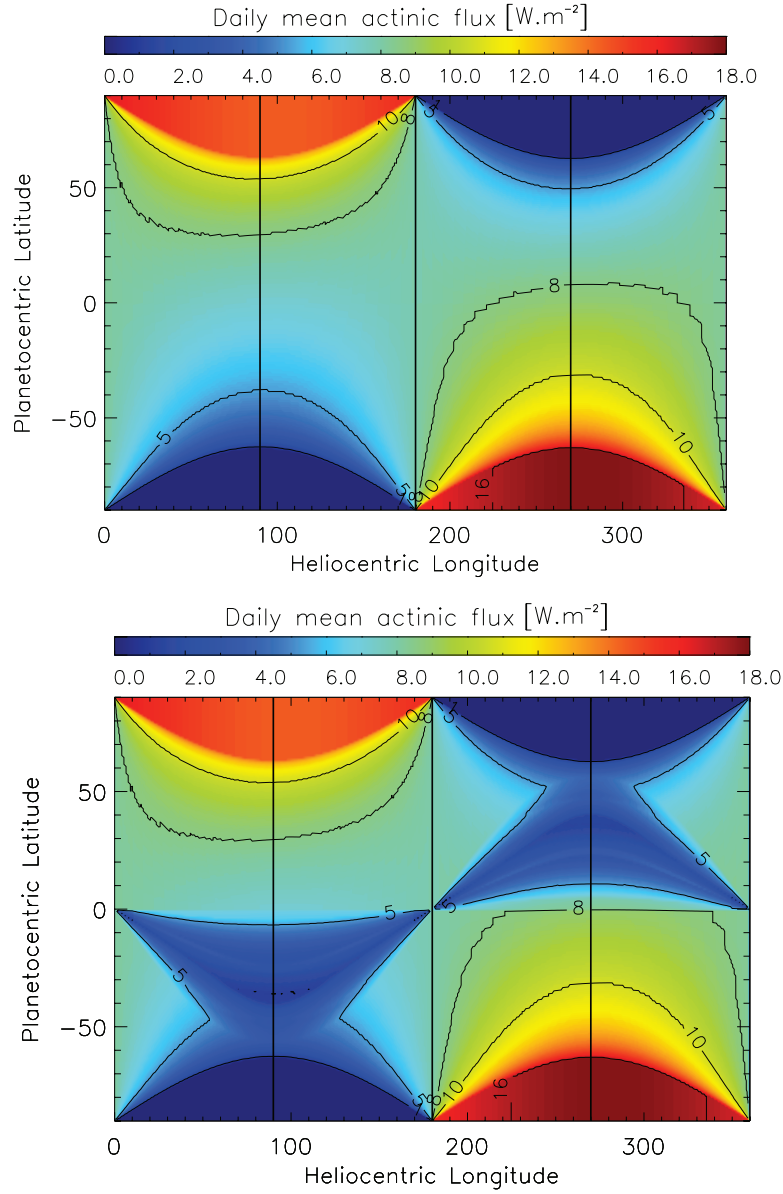
22

Figure 8: Daily mean actinic flux in $[\mathrm{W\,m^{-2}}]$ as a function of planetocentric latitude and heliocentric longitude. Ring shadowing is included in the lower panel. The black solid lines indicate the position of the solstices and equinoxes (see Fig. 1).
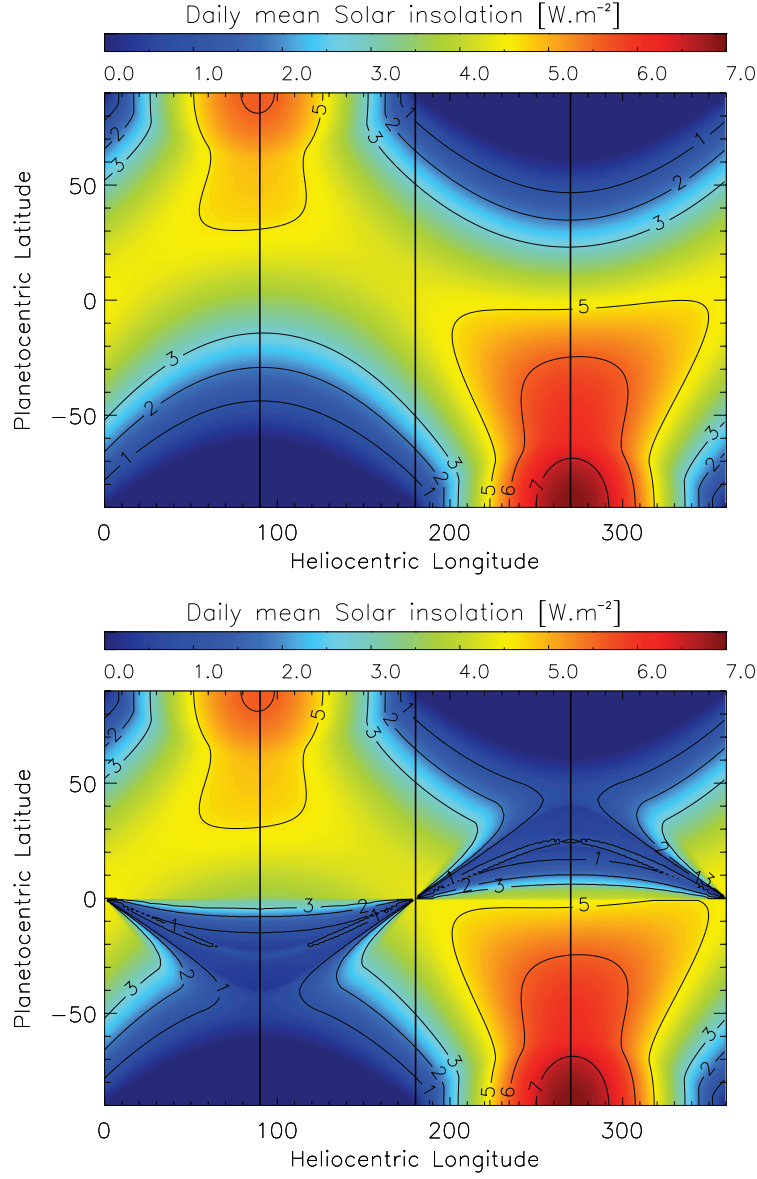
Figure 9: Daily mean insolation in $[\mathrm{W\,m^{-2}}]$ as a function of planetocentric latitude and heliocentric longitude (i.e., seasons) received by a horizontal unit surface in Saturn's atmosphere. Ring shadowing is included in the lower panel. The black solid lines indicate the position of the solstices and equinoxes (see Fig. 1).

C_2H_2 shows a seasonal variability similar to C_2H_6, with some differences arround the 1 mbar pressure level, because C_2H_2 has substantial production at this pressure level by reactions R6 ($H + C_2H_3 \rightarrow C_2H_2 + H_2$) and R21 ($C_2H + H_2 \rightarrow C_2H_2 + H$), and depletion by R5 ($H + C_2H_2 \rightarrow C_2H_3$) and R48 ($C_2H_2 + h\nu \rightarrow C_2H + H$).
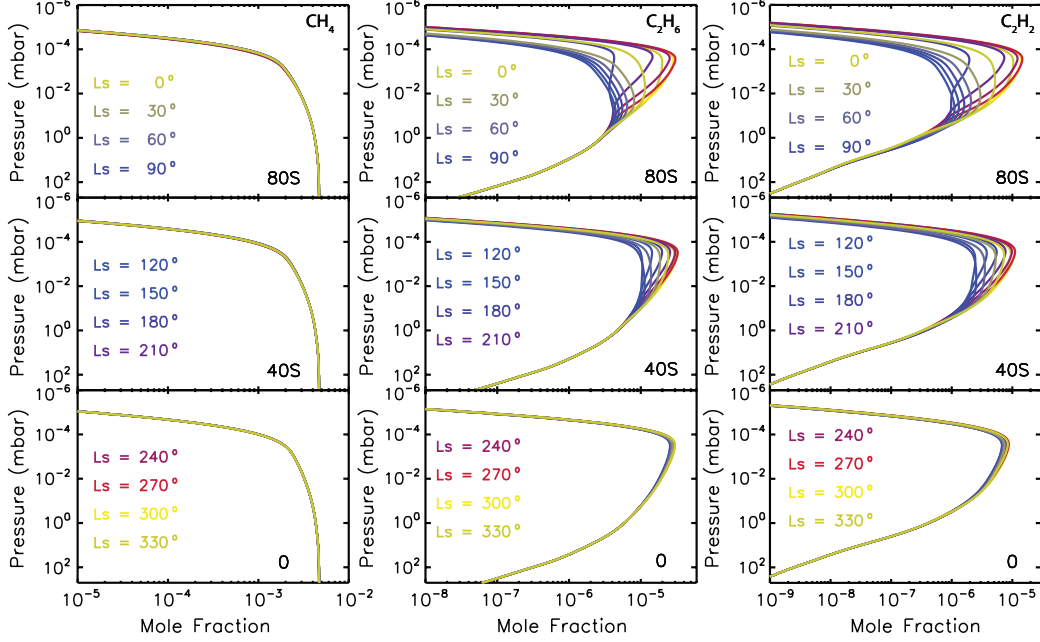
Figure 10: Seasonal evolution of CH_4 (left), C_2H_6 (center) and C_2H_2 (right) vertical profiles computed for the whole Kronian year ($360°$ in heliocentric longitude using a $30°$ step). Three latitudes are presented: $80°S$ (top), $40°S$ (middle) and the equator (bottom). CH_4 does not show any strong seasonal variability, even at high latitudes. Its shape is controlled by vertical mixing rather than photolysis (Romani and Atreya, 1988). The seasonal variability on C_2H_6 and C_2H_2 is clearly seen at low-pressure levels and high latitudes due to the large insolation variation at such latitudes over one Kronian year. The (U) thermal field has been used for these calculations.

4.1.2. Evolution of the C_2H_2 column density

The C_2H_2 column densities computed for pressures lower than 10^{-3} mbar, 10^{-2} mbar, 0.1 mbar and 1 mbar are presented in Fig. 11 , as a comparison with Fig. 8 of Moses and Greathouse (2005). The results concerning the temporal evolution of this column density are in good agreement. The differences

in the column density absolute values can be attributed to differences in the temperature/pressure background, the eddy diffusion profile or the chemical network. At 10^{-3} mbar, an asymmetry between northern and southern summer solstices is caused by Saturn's eccentricity. The maximum value in column density is reached around the southern summer pole, shortly after the southern summer solstice, at $L_s \approx 280°$. The signature of the rings is clearly visible at low latitudes near the solstices in the winter hemisphere. The amount of radicals (and therefore chemical compound produced from radicals) is reduced (see for instance Edgington et al. 2012) due to the partial absorption of the UV radiation by Saturn's rings. At higher pressure levels, the ring signature is damped, and disappears almost completely at 0.1 mbar. From that pressure level to higher ones, the abundance of C_2H_2 is mainly controlled by the downward diffusion of C_2H_2 produced at lower pressure levels. Therefore, from that pressure level, the column density features (e.g., maxima and minima) are increasingly phase-lagged with increasing pressure. These plots also show that the maximum value of the C_2H_2 column density is shifted from high latitudes to equatorial latitudes with increasing pressure in agreement with previous work of Moses and Greathouse (2005). Indeed, this column density mimics the seasonal solar actinic flux at high altitudes (around 10^{-3} mbar), while it follows the annually averaged actinic flux at lower altitudes (at 1 mbar and below) where the column density is maximum at the equator.

4.1.3. Other species

The seasonal evolution of the vertical profiles of several other compounds of interest are presented in Fig. 12 for 80°S, where variability is expected to be most noticeable. Radicals, such as atomic hydrogen (H) and methyl (CH_3), show a strong seasonal variability, as they mainly result from the photolysis of CH_4 and depend therefore on insolation conditions. These short-lived radicals undergo a drastic decrease in their abundances in winter conditions at this latitude, i.e., when CH_4 photolysis is stopped by the polar night. Ethylene (C_2H_4) also shows significant seasonal changes around 10^{-4} mbar as they mainly result from reactions involving CH radicals and methane (R13: $CH + CH_4 \rightarrow C_2H_4 + H$). Below that level, C_2H_4 production rate through reaction R7 ($H + C_2H_3 \rightarrow C_2H_4$) becomes increasingly important, consistently with Moses and Greathouse (2005), to be its main production process around 1 mbar.

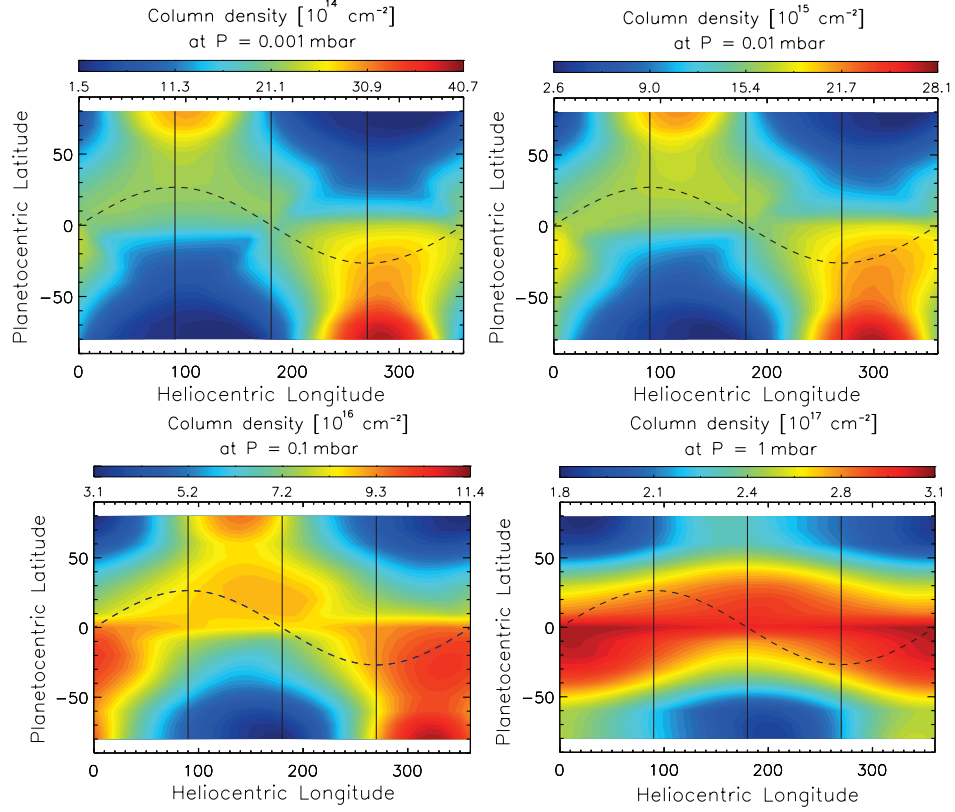Figure 11: C_2H_2 column density $[cm^{-2}]$ above 10^{-3} mbar (top left), 10^{-2} mbar (top right), 0.1 mbar (bottom left), and 1 mbar (bottom right). Ring shadowing is clearly seen around the winter solstice in the winter hemisphere. The solid line indicate the solstices and equinoxes, while the dashed line indicates the position of the subsolar point along the year. The North-South asymmetry between the summer hemispheres is caused by Saturn's eccentricity, its perihelion occurring shortly after the southern summer solstice. In both summer hemispheres, after the summer solstice, the C_2H_2 column densities reach a maximum which is shifted in time with respect to the maximum insolation level, i.e. at the solstice itself.

27
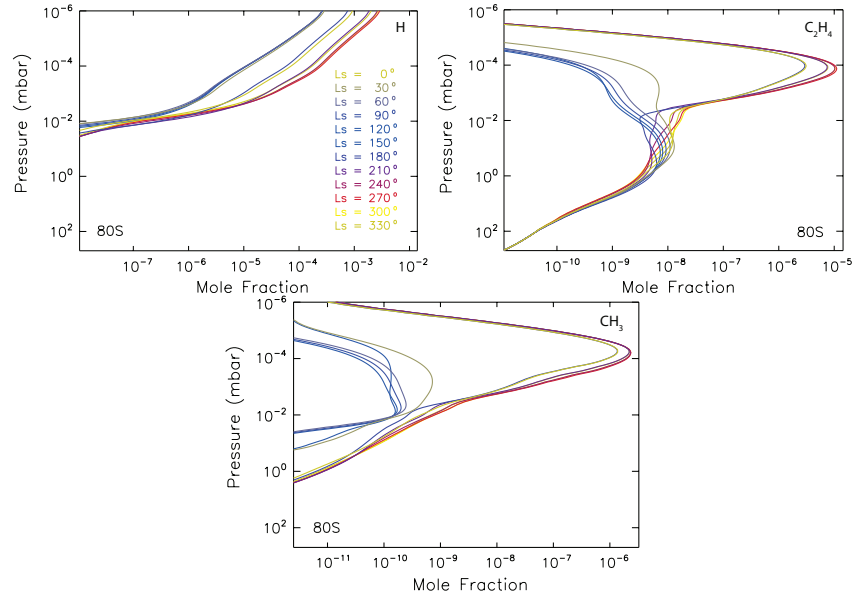
Figure 12: Seasonal evolution of the mole fraction of atomic hydrogen (H, top left), ethylene (C_2H_4, top right), methyl (CH_3, bottom) as a function of pressure and heliocentric distance (L_s) at 80°S. The profiles are presented using a 30° step in L_s.

4.1.4. Impact of the rings on chemistry

The impact of the UV absorption by the rings on the seasonal evolution of C_2H_2 and C_2H_6 mole fractions are depicted in Fig. 13 and 14. As expected from geometrical considerations, and given the latitudinal extent of the numerical cells of the model, the ring shadowing effect is maximum at latitudes below 50° in the winter hemisphere, at the solstice itself, i.e. when the shadow cast by the ring on the planet are the most extended in that hemisphere. The impact of the ring shadowing is more localised in time at a latitude of 40° than at a latitude of 20° in the winter hemisphere. At these latitudes, the main impact on chemistry of the ring shadowing effect comes from Saturn B ring. At a latitude of 20° in the winter hemisphere, the ring shadowing effects are effective over 140° in L_s, while at a latitude of 40°, they are effective over 80° in L_s. At higher pressure levels, and similarly to the column density, the mole fraction minima and maxima are damped and phase-lagged.

4.2. Accounting for the seasonal temperature field

In this section, we present results from the seasonal simulations using the seasonal (S) thermal profiles. The vertical profiles of CH_4, C_2H_6, and C_2H_2, using this thermal field are displayed in Fig. 15. These profiles have to be compared with Fig. 10, where the (U) thermal field was used.

Taking the (S) field into account leads to differences with respect to the (U) case in the amplitude of the seasonal variability of C_2H_2 and C_2H_6 at pressure levels ranging from 10^{-5} to 10^{-1} mbar. C_2H_2 now shows a small seasonal variability at pressure levels ranging from 0.5 to 10 mbar, which was not the case previously. The position of the homopause is also expected to vary, as the molecular diffusion coefficient has a thermal dependency ($D_i \propto T^{1.75}/p$). Using the (S) field, the homopause is generally shifted to a lower pressure, due to the fact that the (U) thermal field corresponds to summer conditions at latitude of 20° in the summer hemisphere.

The seasonal evolutions of the C_2H_2 and C_2H_6 mole fractions at three pressure levels (10^{-4}, 10^{-2} and 1 mbar) and considering the (S) and (U) thermal fields are shown in Figs. 16, 18 and 20. For the sake of comprehension, the seasonal evolution of temperatures at these same pressure levels are shown alongside as well as the position of the different solstices and equinoxes. We only present these seasonal evolutions at a few latitudes in the southern hemisphere, although the same occurs in the northern hemi-
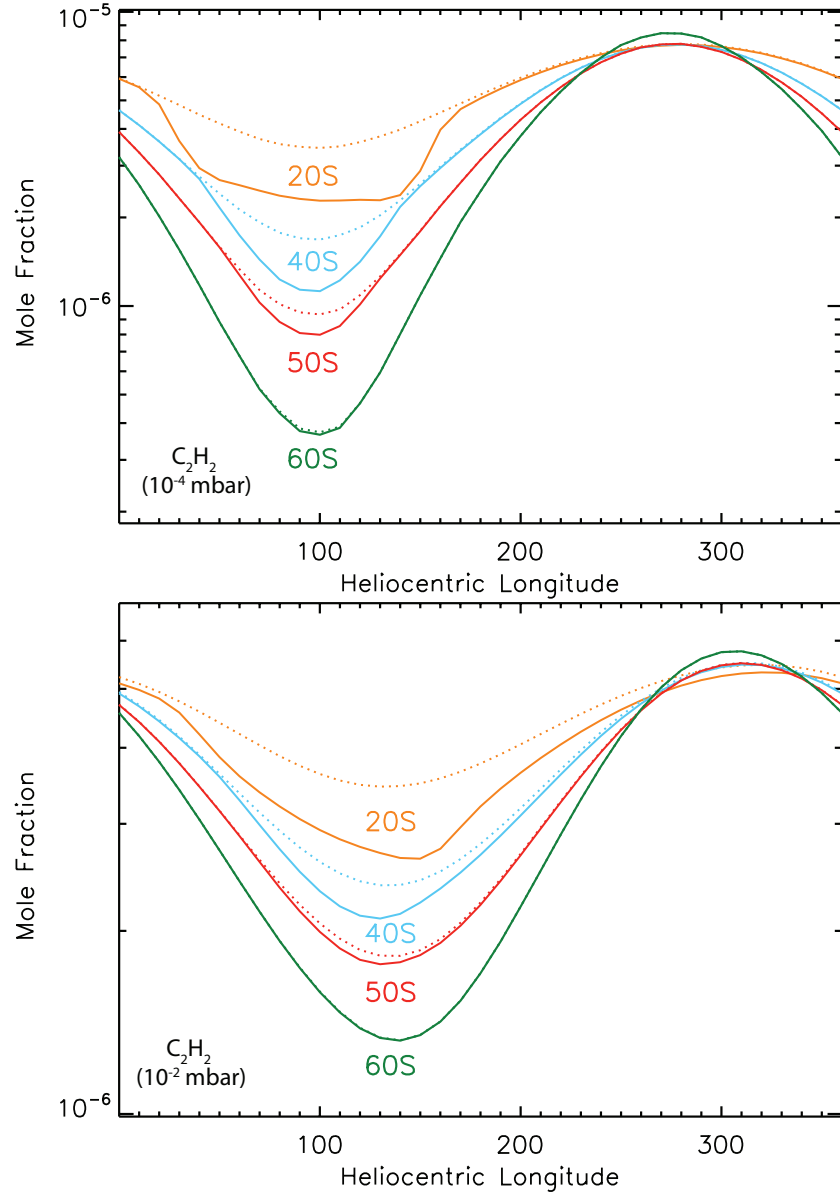
29

Figure 13: C_2H_2 mole fraction at 10^{-4} mbar (top) and 10^{-2} mbar (bottom) as a function of heliocentric longitude. The solid lines include ring-shadowing effects, whereas the dotted lines do not include this effect. These effects are only visible from the equator to $\pm 50°$. High latitudes are alternately in polar day and polar night. The mole fraction minima and maxima are damped and phase-lagged at 10^{-2} mbar with respect to 10^{-4} mbar.
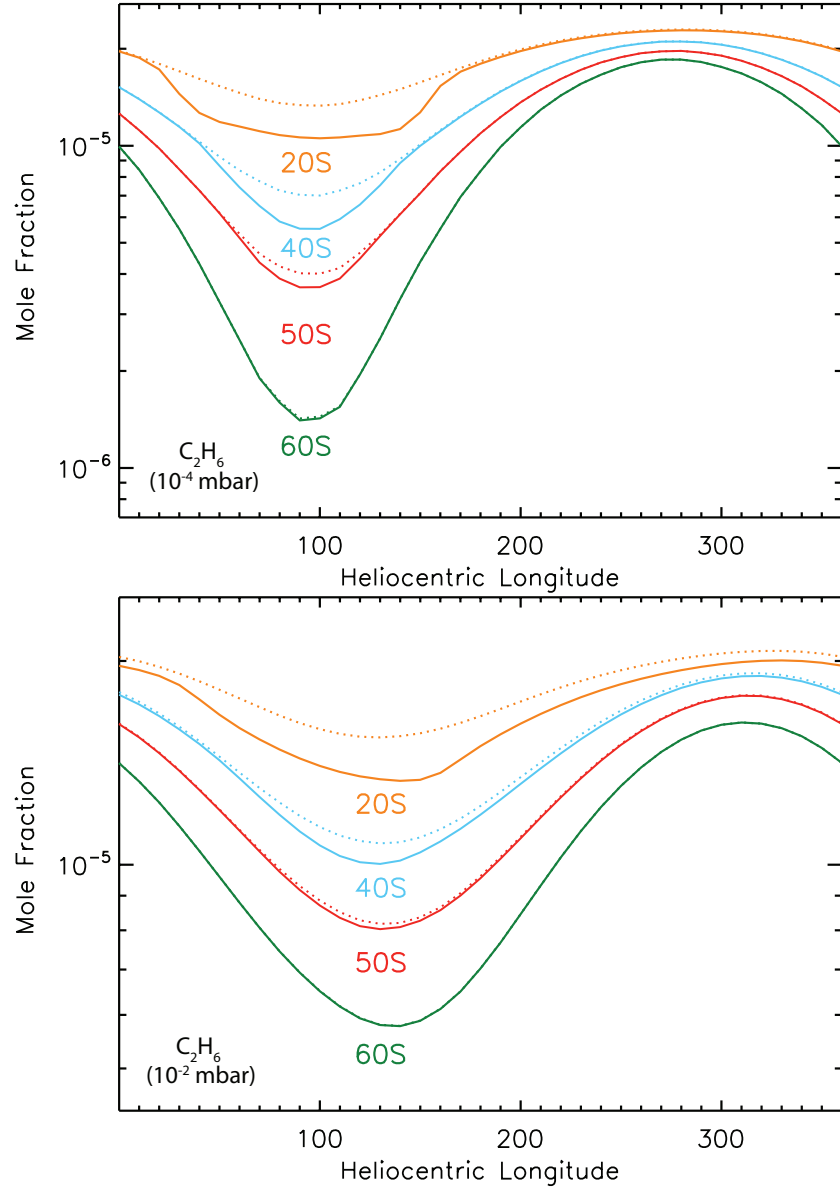
Figure 14: Same as Fig. 13 for C_2H_6. Solid and dotted lines represent photochemical predictions with and without ring shadowing, respectively.
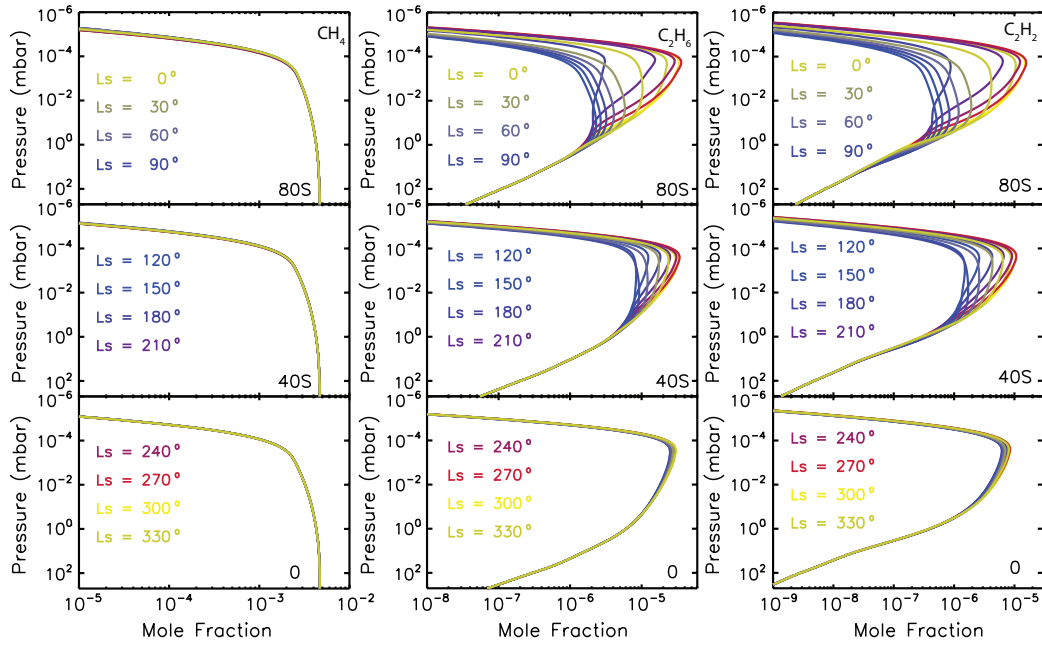
Figure 15: Seasonal evolution of CH_4 (left), C_2H_6 (center) and C_2H_2 (right) vertical profiles computed for the whole Kronian year ($360°$ in heliocentric longitude using a $30°$ step) and using the seasonal (S) thermal field.

sphere. Therefore, in what follows, summer and winter refer to these seasons in the southern hemisphere, if not otherwise specified.

• **Fig. 16:** At 10^{-4} mbar, C_2H_2 and C_2H_6 mole fractions, as predicted using both (S) and (U) thermal fields, evolve in phase. Around the summer solstice ($L_s = 270°$), the abundance of these compounds is increased when considering the (S) thermal field and they both show a positive abundance gradient from the equator to the south pole. Note that, when considering the (U) field, C_2H_6 shows a very small abundance gradient at the summer solstice.

The differences in C_2H_2 and C_2H_6 abundances between both (S) and (U) thermal field calculations never exceed 50% except at high latitudes at summer solstice where C_2H_2 and C_2H_6 abundances are enhanced by a factor of 1.3 and 1.6, respectively. The small bump observed at the equator with both thermal fields is due to the absence of ring shadowing due to the thin nature of the rings. The ring opacity on the UV field is averaged over the latitudinal extent of the numerical cells, which are 10°-wide here. A local maximum on the UV field is expected at the equator at $L_s = 0°$ and 180°, i.e. when the projection of the rings over Saturn's planetary disk is negligible, given the latitudinal extent of the numerical cells. The temperatures at 40°S for L_s ranging from 50° to 140° vary abruptly with times due to the shadowing from the different rings. The temperature of the (U) thermal field at this pressure level is 1 K warmer than the one of (S) thermal field at latitude of 80°S around the summer solstice.

At 10^{-4} mbar, the C_2H_2 production is mainly controlled by reactions R50 ($C_2H_4 + h\nu \rightarrow C_2H_2 + H_2$) and R51 $C_2H_4 + h\nu \rightarrow C_2H_2 + H + H$) as displayed on Fig. 17 (left panel). The integrated production rates above that pressure level computed using the (S) thermal field are always greater than the ones computed with the (U) field. These differences are caused by the temperature which affects the position of the homopause and allows the UV radiation to penetrate deeper in the (U) thermal field case. This ultimately leads to an increase in the integrated production rate above 10^{-4} mbar of CH radical from methane photolysis. Since the (U) thermal field is hotter than the (S) thermal field at all times along the year, the integrated production rates of C_2H_2 and C_2H_6 above 10^{-4} mbar in the former case are always expected to be greater than the (U) case. From this radical, C_2H_4 is produced through reaction R13, and then photolysed through reactions R50 and R51. We note that the differences in the integrated production rates between these two thermal fields reach a minimum at 40°N around the northern winter sol-

33

stice ($L_s = 270°$) while, at the same time, the C_2H_2 mole fraction becomes more important when considering the (U) thermal field than when using the (S) thermal field. These differences are produced by the decrease in the diffusion timescale due to the contraction of the atmospheric column which cools down around the winter solstice as explained below.

A similar behavior is observed for C_2H_6 (Fig. 17, right panel) whose integrated production rates are controlled by reaction R20. We can however note that, at 80°S and around the winter solstice ($L_s = 90°$) the integrated production rate considering the (S) thermal field is more important than the one using (U) thermal field, consistent with the predicted greater abundance of C_2H_6 at that time.

• **Fig. 18:** At 10^{-2} mbar, C_2H_2 is less abundant at every latitude when the (S) field is accounted for. Its abundance gradually increases with latitude from the equator to the south pole during the summer season. However, at this pressure level, the peak in the C_2H_2 and C_2H_6 abundances during summer is occuring earlier at high latitudes than at mid-latitudes due to Saturn's obliquity. C_2H_6 becomes as abundant with the (S) thermal field as it was with the (U) thermal field during the summer season. A slight dephasing is noted between the two thermal field calculations when C_2H_2 and C_2H_6 reach both their maximal and minimal values. At 80°S, the abundance of C_2H_2 and C_2H_6 is decreased by a factor 2.2 and 1.7, respectively, during the winter season when we consider the (S) thermal field. At this pressure level, the temperatures of the (U) field are 2 K and 6 K warmer than the temperatures of the (S) field at the summer solstice and the winter solstice respectively.

The C_2H_2 production is mainly controlled by reaction R6. The seasonal evolution of the integrated production rate of this reaction above this pressure level is presented in Fig. 19 (left panel) at latitudes of 80°S and 40°N. Around the summer solstice ($L_s = 270°$ for 80°S and $L_s = 90°$ for 40°N), the integrated production rate of reaction R6 in the (U) and (S) cases are very similar, consistent with the predicted C_2H_2 mole fraction. Around the winter solstice ($L_s = 90°$ for 80°S and $L_s = 270°$ for 40°N), the (S) integrated production rate is higher than the (U) one, also consistent with the predicted C_2H_2 mole fractions.

Similarly to the situation at lower pressure levels, the integrated C_2H_6 production rate (Fig. 19, right panel) is controlled by reaction R20. The integrated production rates of this reaction are very similar between the two thermal field cases, all along the year except around the southern winter

solstice at high latitudes. Indeed, the integrated production rate become less important in the (S) case than in the (U) case.

At this pressure level, the differences between the two thermal field cases observed in the C_2H_2 and C_2H_6 abundances are mainly controlled by two quantities. First, a higher integrated production rate above that level will produce a greater quantity of the considered molecule. At the same time, the contraction of the atmospheric column during the winter season will increase the diffusion of the produced hydrocarbons to higher pressure levels. This former effect is clearly noticed for C_2H_6 at 40°N during the northern winter season where its integrated production rate above that level with the (S) thermal field is slightly greater than the one with the (U) thermal field, while its predicted abundance is lower in the (S) case than in the (U) case.

• **Fig. 20:** At 1 mbar, C_2H_2 still shows seasonal variability while C_2H_6 seasonal variability is negligible with the (U) thermal field. The variability of these compounds persists at higher-pressure level when the (S) thermal field is accounted for. The dephasing between the two thermal field calculations which was observed at 10^{-2} mbar is now enhanced here. C_2H_6 is more abundant at the equator using the (S) field, and has now a steeper abundance gradient toward the South pole. The temperature of the (U) field corresponds to temperatures of the (S) field at 40°S during the winter solstice.

Note that the resolution of the model in the pressure space varies with thermodynamic conditions as discussed in 2.3.2, while the vertical resolution of the model is constant. The altitudinal resolution of the model has been doubled in order to assess if the differences observed between the two thermal fields at high latitudes in the winter hemisphere where not due to numerical artifact. The results obtained were identical.

It is clear from Figs 18 and 20 that accounting for the (S) thermal field leads to a decrease in the seasonal lag of C_2H_6 and C_2H_2 at pressure levels higher than 10^{-2} mbar. We also noted that these two compounds still show seasonal variability at 1 mbar while this variability has already vanished for C_2H_6 with the (U) thermal field. The temporal positions of the maximum and minimum abundance values as a function of pressure, corresponding to summer and winter conditions (hereafter called summer peak and winter hollow, respectively), are displayed in Fig. 21. We note an increase in the phase lag between the (U) and the (S) thermal field calculations with increasing pressure from the 10^{-2} mbar to the 1 mbar pressure level. At 1 mbar, the depletion in the C_2H_6 abundance due to low-insolation winter conditions (winter hollow) is occurring 60° in heliocentric longitude earlier with the
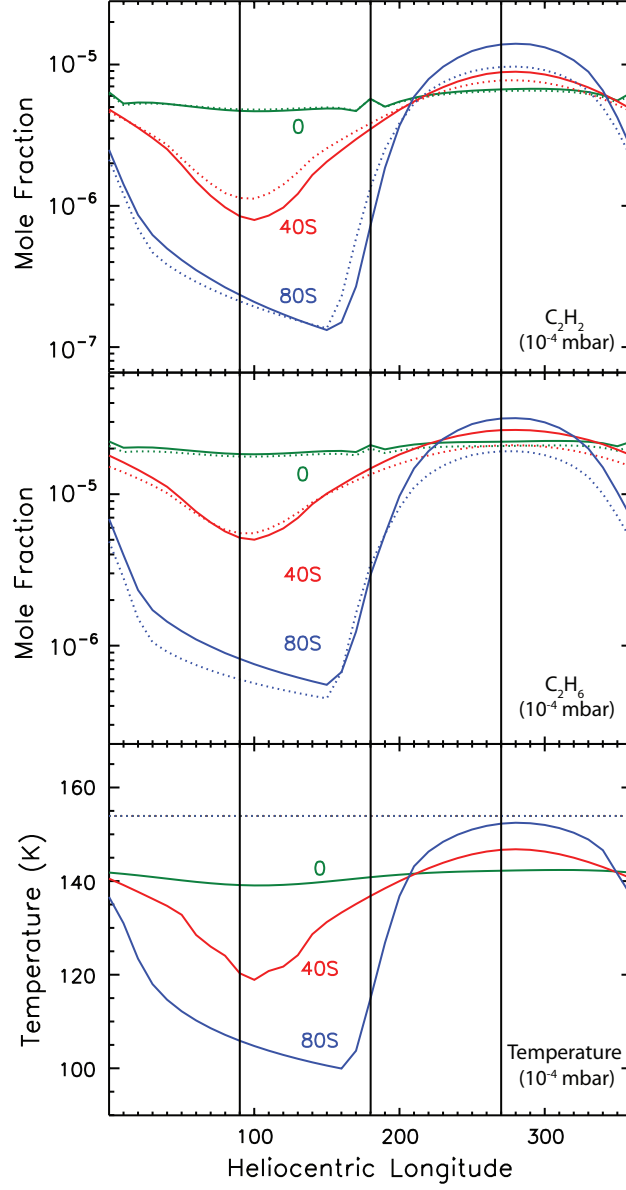
Figure 16: Evolution of the C_2H_2 mole fraction (top panel), the C_2H_6 mole fraction (middle panel) and temperature (bottom panel) at 10^{-4} mbar. The evolution of mole fractions and temperature is plotted as a function of heliocentric longitude for latitudes of 80°S, 40°S and at the equator. Values obtained with the (S) and (U) thermal fields are displayed with solid and dotted lines, respectively. The black solid lines indicate the position of the solstices and equinoxes (see Fig. 1).
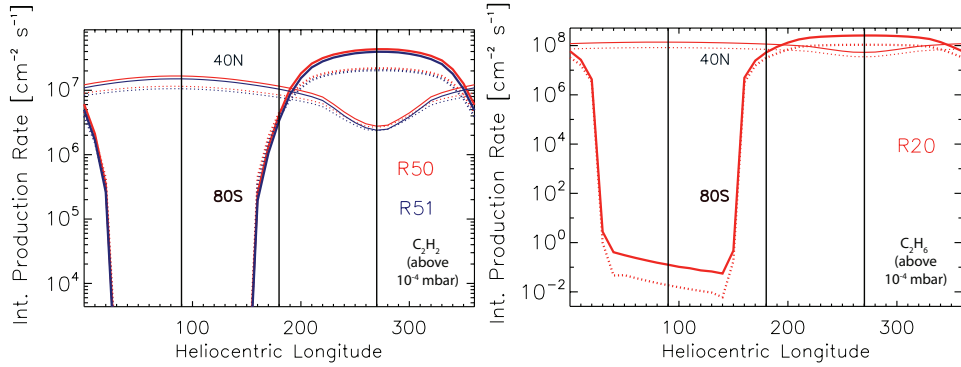
36

Figure 17: Seasonal evolution of the integrated production rate above 10^{-4} mbar of the main reactions leading to the production of C_2H_2 (left panel) and C_2H_6 (right panel). For the sake of clarity these integrated production rates are presented at $80°S$ (thick lines) and $40°N$ (thin lines). Calculations that include the (S) and (U) thermal field are displayed with solid and dotted lines, respectively.

(S) thermal field than with the (U) thermal field. Similarly, the increase in C_2H_6 abundance due to summer conditions (summer peak) is occurring $40°$ in heliocentric longitude earlier.

We can note here some discrepancies between both our study cases and the following statement previously made by Moses and Greathouse (2005): "Our assumption of a constant thermal structure with time and latitude introduce mole-fractions errors of a few percent but will not affect our overall conclusions." This statement seems to be clearly in disagreement with the results presented in Figs. 16, 18 and 20 where the differences between the (U) and (S) cases are well beyond a few percent. The fact that we did not reach the same conclusions lies in the different approach we had. In the present model, we assumed that the compounds mole fractions followed the atmospheric contraction/dilatation in the pressure space with changing thermodynamic conditions (see 2.3.3). Therefore, when the atmosphere column contracts, the mole fraction vertical gradients in altitude are increased and the diffusion to higher pressure levels becomes faster. On the other hand, when the thermal structure does not evolve with time (i.e. the (U) study case), our approach is identical to the work of Moses and Greathouse (2005).

The diffusion timescale is therefore decreased at all times in the (S) model with respect to the (U) model, due to the thermal evolution of the (S) model. Consequently, this decrease in the diffusion timescale shifts to higher pres-
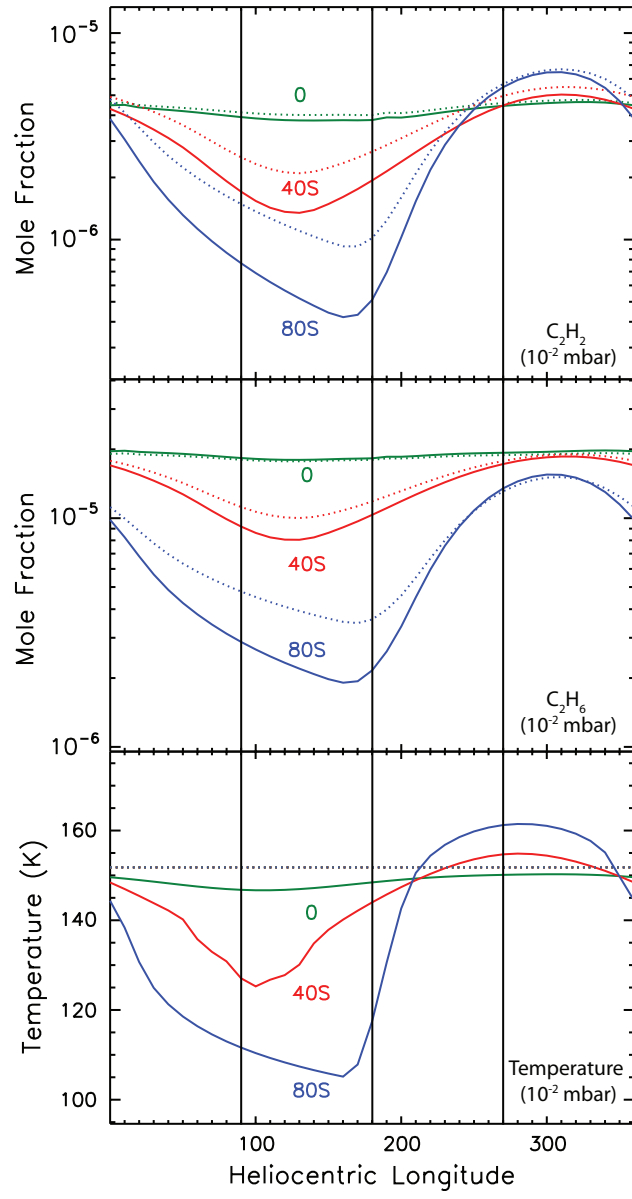
37

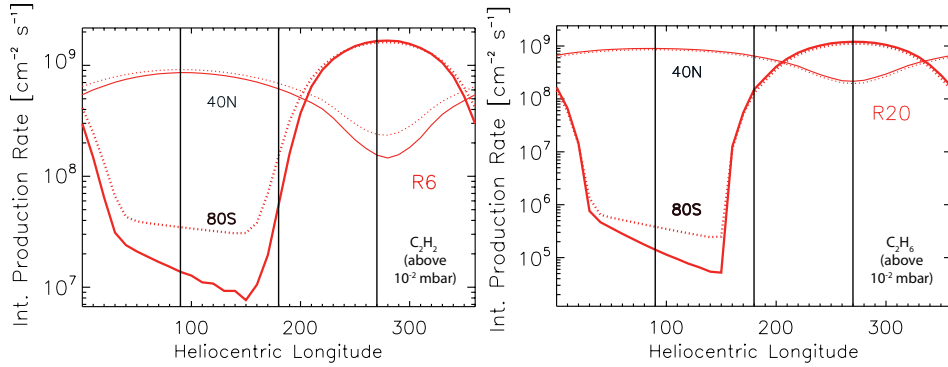Figure 18: Same as Fig. 16 at 10^{-2} mbar.

Figure 19: Same as Fig. 17 for 10^{-2} mbar.

sures the level where the seasonal variations vanish. This effect is maximized at the poles where the seasonal variations in temperature are important.

We remind the reader that we assumed a seasonally and latitudinally constant eddy diffusion profile, due to the lack of constraint on this free-parameter.

5. Comparison with Cassini/CIRS data

After Cassini's arrival in the Saturn system, observations of hydrocarbons have been performed with an unprecedented spatial and temporal coverage, either with nadir (Howett et al., 2007; Hesman et al., 2009; Sinclair et al., 2013) or limb (Guerlet et al., 2009, 2010) observing geometries. Howett et al. (2007) reported the meridional variability of C_2H_6 and C_2H_2 from 15°S to almost 70°S at a pressure level around 2 mbar between June 2004 ($L_s \approx 292°$) and November 2004 ($L_s \approx 298°$) with Cassini/CIRS. The C_2H_2 distribution was found to peak around 30°S and decreases towards both the equator and the South Pole. C_2H_6 showed a rather different and puzzling behavior, with an increasing abundance southward from the equator, confirming the earlier findings of Greathouse et al. (2005) and Simon-Miller et al. (2005).

Sinclair et al. (2013) reported observations of C_2H_6 and C_2H_2 around the 2.1 mbar pressure level, acquired in nadir observing mode with a good spatial coverage, from South to North Pole. These observations range in time from March 2005 ($L_s \approx 307°$) to September 2012 ($L_s \approx 37°$). However, the most recent ones were contaminated with the signature of Saturn's 2011 Great Storm (Fletcher et al., 2011; Fischer et al., 2011; Sánchez-Lavega et al.,
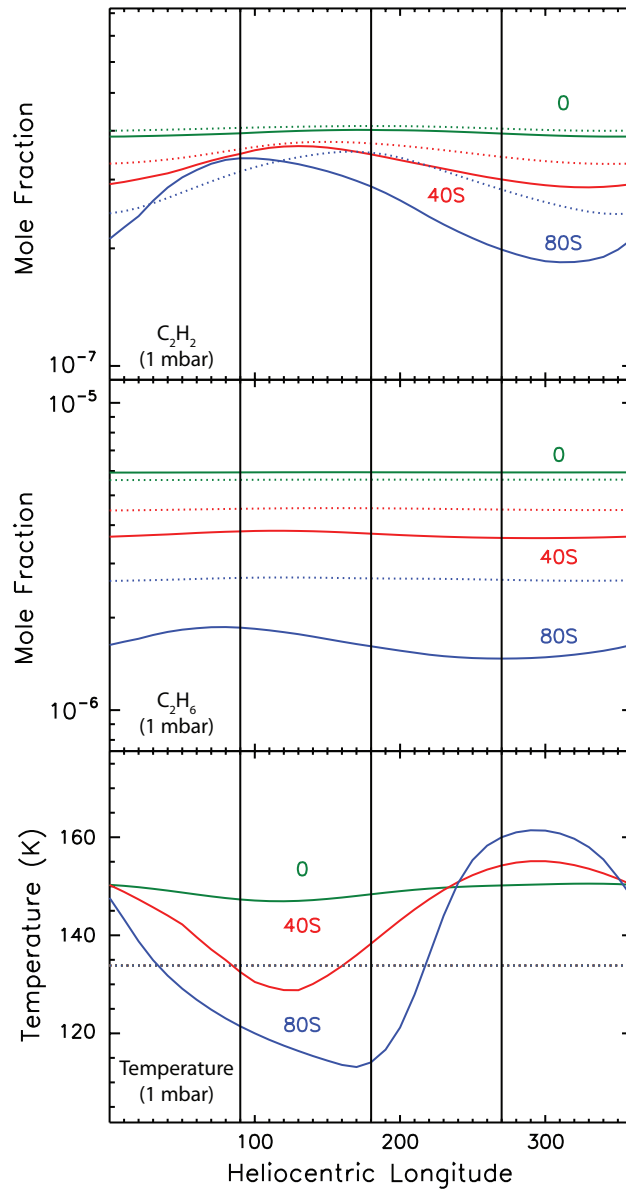
39

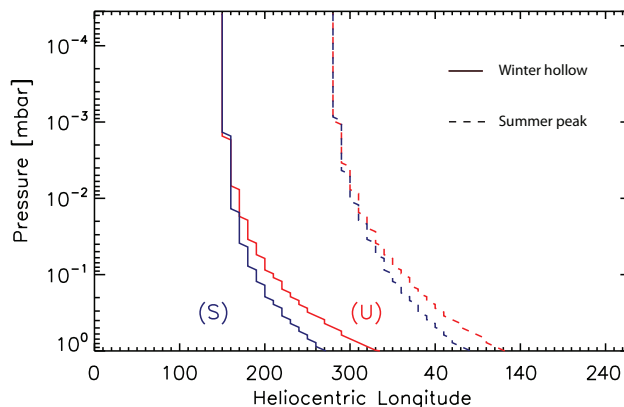Figure 20: Same as Fig. 16 at 1 mbar.

40

Figure 21: Evolution of the seasonal maximum value (*summer peak*, dashed lines) and minimum value (*winter hollow*, solid lines) reached by the C_2H_6 mole fraction as a function of pressure at 80°S. Calculations using the (S) and the (U) thermal fields are denoted by blue and red colors, respectively.

2011), which stratospheric aftermath was studied extensively by Fletcher et al. (2012). Their retrieval suggests that C_2H_2 is abundant at the equator and decreases toward the poles. Similarly to previous findings, C_2H_6 showed a behavior different from C_2H_2. The observed trend suggests an enrichment in C_2H_6 at high southern latitudes.

The observations retrieved by Guerlet et al. (2009, 2010) from Cassini/CIRS limb-scans, enabled constraining the vertical distributions of C_2H_2 and C_2H_6 from 5 mbar to 5 μbar. The retrieved mole fraction meridional profiles of C_2H_2 and C_2H_6 at 1 mbar are presented in Fig. 22 for a better comparison with already published nadir observations (Howett et al., 2007; Sinclair et al., 2013). When considering the meridional profiles only, the systematic errors are not considered and therefore the observational errors have been reduced of 20 % in Fig. 22. We chose not to rescale our predictions to superimpose them to the observations, although it is occasionally observed in the literature. Dobrijevic et al. (2003) and Dobrijevic et al. (2010a) showed that uncertainty propagations in giant planet photochemistry lead to uncertainties of about an order of magnitude in the C2 species' abundances at arround the 1 mbar pressure level. Recent improvement on the chemical scheme greatly reduced these uncertainties (Hébrard et al., 2013; Dobrijevic et al., 2014; Loison et al., 2014) (see Fig. 7) by a factor of 1.8 for C_2H_6 and a factor of 4.2 for C_2H_2. The absolute differences between the photochemical
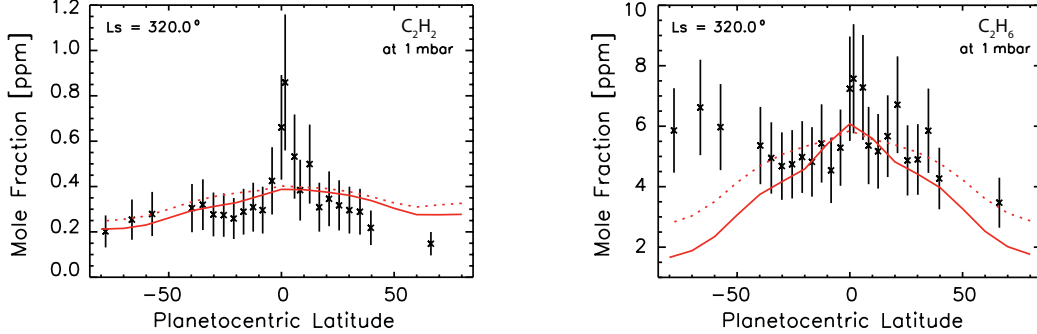
41

Figure 22: Comparison between the Cassini/CIRS limb observations (Guerlet et al., 2009) for heliocentric longitudes ranging from $L_s \approx 300°$ to $L_s \approx 340$ ° and the photochemical model predictions. Photochemical predictions are presented for a heliocentric longitude of 320°. C_2H_2 and C_2H_6 are respectively shown in the left and right panels. Model outputs using the (S) and (U) thermal fields are denoted by solid and dotted lines, respectively. No rescaling factors have been applied, see text for details.

predictions and the observations shall not be seen as a concern if it remains within the photochemical uncertainties. What can (and have to) be compared between observations and models are the general trends seen in the meridional distributions at the relevant pressure levels.

The Cassini limb-observations offer latitude and altitude information. The retrieved abundances of these two molecules over the pressure sensitivity range are presented in Fig. 23 at a few observed planetographic latitudes. We have selected these latitudes in order to display the different features noted when confronting these observations with the model, *e.g.* a large over-prediction of their abundance at high southern latitudes and low pressure level, a good agreement at mid-to-low latitudes, and an under-prediction at mid-to-high northern latitudes and high pressure levels, especially noted for C_2H_6. It is worth presenting a comparison with these data in two-dimensional plots for the sake of clarity. The relative differences between the Cassini observations of C_2H_6 and C_2H_2 from the photochemical predictions using (S) thermal field are displayed in Fig. 24 using a logarithmic scale. The positive and negative values therefore denote the regions where the photochemical model under and over-predicts the abundance of these compounds, respectively. The quantity $log(y_i^{CIRS}/y_i^{PM})$ is plotted as a function of the pressure range and the latitude, where y_i denotes respectively the mole fraction of species i, while PM stands for photochemical model. Because the latitudi-

nal coverage of Cassini limb-observations is limited, we have indicated the latitude of each observation by black vertical lines.

5.1. C_2H_2

At the 1 mbar pressure level (Fig. 22), our photochemical model simulations agree reasonably well with the meridional trend seen in the C_2H_2 meridional profiles, namely the poleward decrease of its abundance, as reported by Guerlet et al. (2009, 2010) and Sinclair et al. (2013). Differences are observed in the equatorial regions, at latitudes lower than 15° and Northward of 35°N.

Below the 0.1 mbar pressure level (see Fig. 24), the agreement with the C_2H_2 distribution reported by Guerlet et al. (2009) is within the uncertainty range of the observations from the equator to ± 40°. The agreement is however poor at lower-pressure levels and high-southern latitudes, where C_2H_2 abundance tends to be over-predicted.

In the equatorial zone, the differences between our photochemical predictions and the observations change sharply over a short latitudinal range. Fig. 22 shows that our model does not reproduce the equatorial peak of C_2H_2 abundance (between 5°S and 5°N roughly). This peak is thought to be caused by Saturn's thermal Semi-Annual Oscillation (SSAO) (Orton et al., 2008; Fouchet et al., 2008; Guerlet et al., 2009, 2011).

In the southern hemisphere, from 10°S to 40°S, we over-predict the C_2H_2 mole fraction at pressures lower than 0.1 mbar. This feature is also observed when comparing C_2H_6 predictions to observations and is discussed below.

5.2. C_2H_6

Moses and Greathouse (2005) have shown that the seasonal variability of C_2H_6 at pressures higher than 0.8 mbar was negligible, because the timescale driving this compound's abundance becomes longer than the Saturn year below that pressure level.

Due to the larger chemical evolution timescale of C_2H_6 with respect to C_2H_2, this compound is expected to be more sensitive to transport processes than the latter one. In addition to that, the uncertainties on the reactions involved in the production or destruction of C_2H_2 lead to an important error bar on its vertical profile (recall Fig. 7), whereas the predicted shape of C_2H_6 has smaller error bars. Therefore, C_2H_6 is a compound that should be first used to trace dynamics rather than C_2H_2. C_2H_6 is reasonably well reproduced from the equator to 40° in both hemispheres below the 0.1 mbar pressure
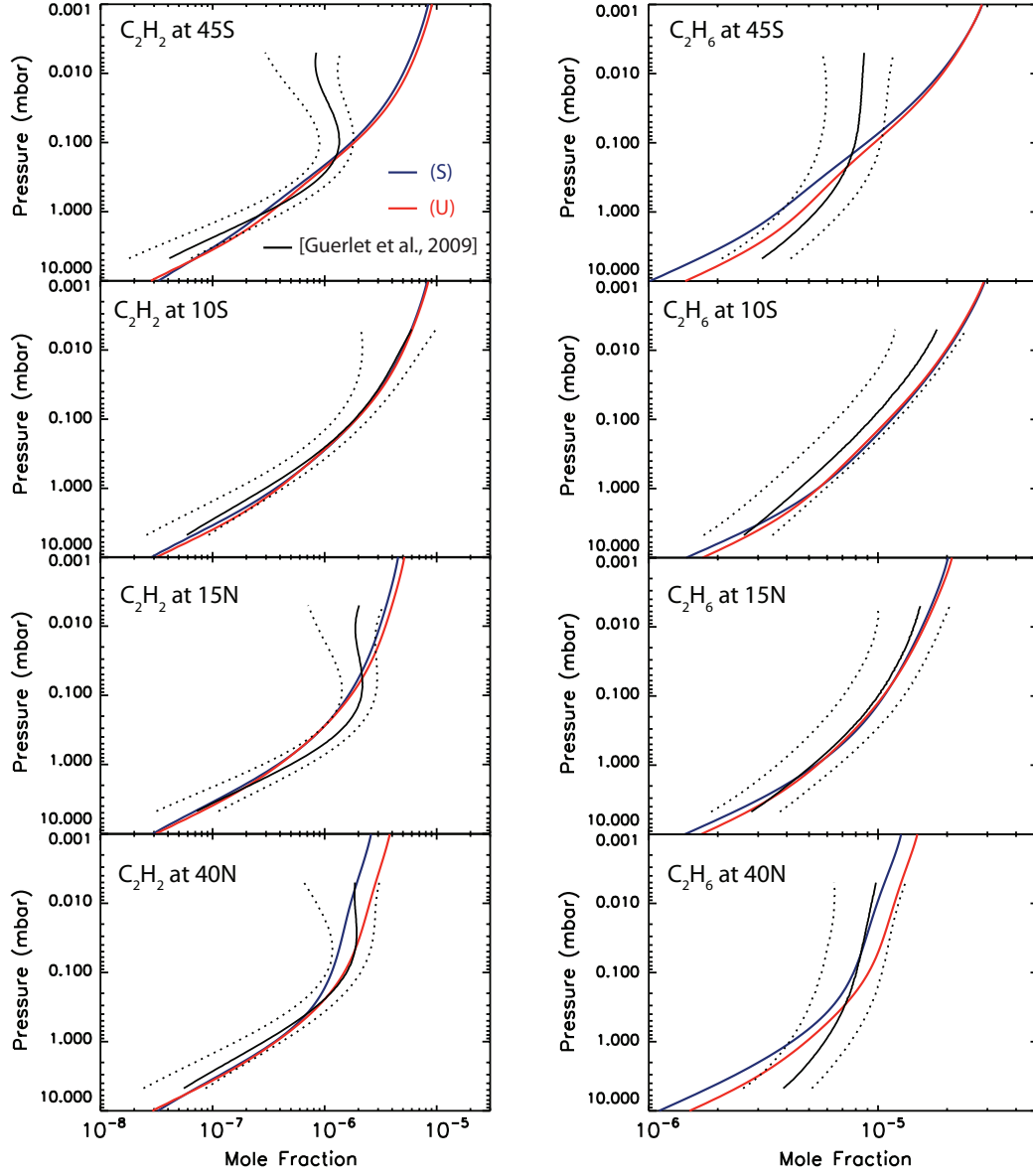
Figure 23: Comparison between the C_2H_2 (left panels) and C_2H_6 (right panel) retrieved abundances with the photochemical predictions over the pressure sensitivity range at few observed planetographic latitudes. Photochemical predictions that uses the (S) and (U) thermal field are displayed by solid blue and red colors, respectively. Solid and dotted black lines represent the observed abundances of Guerlet et al. (2009) with the 1-σ uncertainties, respectively. Photochemical predictions are presented for a heliocentric longitude of 320°.
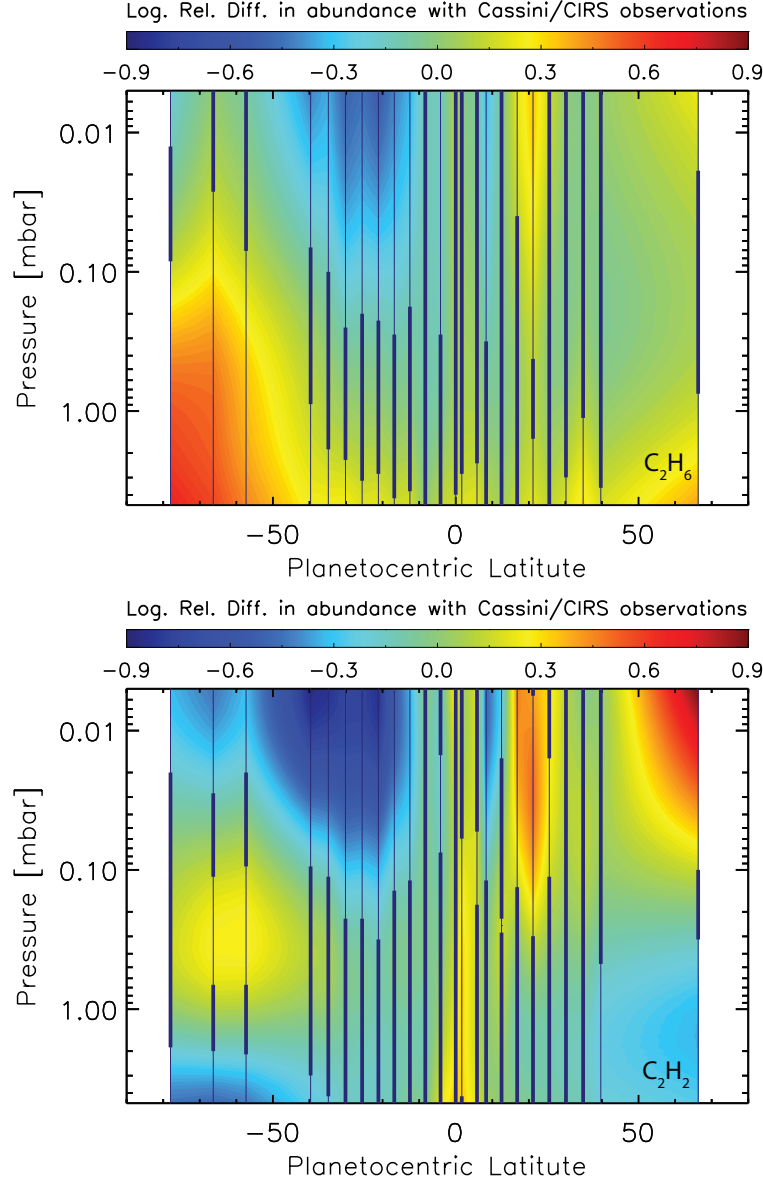
44

Figure 24: Comparison between observations (Guerlet et al., 2009) and photochemical predictions as a function of the pressure sensitivity range of limb observations and planetocentric latitudes. C_2H_6 and C_2H_2 are presented in the upper and lower panel, respectively. The observing period ranges from $L_S = 300°$ and $L_S = 340°$. Observations are compared to photochemical predictions at $L_S = 320°$. The logarithm of the difference between Cassini observations of these compounds and the photochemical predictions that use (S) thermal field is plotted here. Positive/negative values denote an under/over-prediction of the photochemical models. The vertical lines denote the latitudes for which observations have been made. The thick portions of those lines show the region where the photochemical predictions are within the observation uncertainties. Uncertainties on the photochemical predictions are not taken into account. No scaling factor have been applied.

45

level. An equatorial peak similar to the one observed in the C_2H_2 meridional profile (see Fig. 22), though with a smaller relative amplitude, is present in the C_2H_6 meridional profile and could also be caused by the SSAO. Similarly to C_2H_2, we underpredict C_2H_6 abundance from 40°S to south pole below the 0.1 mbar pressure level, and we overpredict its abundance at latitudes ranging from 10°S to 40°S above the 0.1 mbar pressure level. These similar over/underprediction seen in C_2H_2 and C_2H_6 could be caused by large scale dynamical cell redistributing species meridionally in Saturn's stratosphere, as suggested by Guerlet et al. (2009, 2010), Sinclair et al. (2013).

At the 1 mbar pressure level (Fig. 22), the photochemical predictions that use the (S) thermal field predict a steeper equator-to-pole gradient, which arise from the faster diffusion to higher-pressure levels when considering the (S) thermal field. Fitting these meridional profiles with dynamical processes could help to constrain meridional mixing processes and will be the object of a forthcoming study.

5.3. Does accounting for the seasonal evolution of the thermal field better fit Cassini data?

Fig. 25 presents the comparison between Cassini-limb observations with photochemical predictions using the (U) thermal field in a similar way as Fig. 24. C_2H_6 is better predicted using (U) thermal field below 1 mbar while C_2H_2 is better predicted at all pressure levels using (S) thermal field. The region where C_2H_6 was widely under-predicted with the (S) thermal field from mid-southern latitude to South pole (recall Fig. 24), is now sligthly reduced, but it remains significant.

The evolution of the Chi-Square goodness-of-fit between the predicted C_2H_2 and C_2H_6 abundance (using both thermal fields) and Cassini observations for every observed latitudes is shown in Fig. 26. These values are computed first by interpolation of the photochemical prediction on the observed latitudes and pressure levels, then the Chi-Square coefficient presented in Fig. 26 is computed and summed over the observed latitudinal range. Using the (S) thermal field in the predicted C_2H_6 profile represents a slight improvement at pressures lower than 0.2 mbar. However, in the lower stratosphere, from 0.2 mbar to 5 mbar, the predicted C_2H_6 shape is better reproduced using the (U) thermal field. C_2H_2 is better reproduced using the (S) thermal field at all pressure levels.
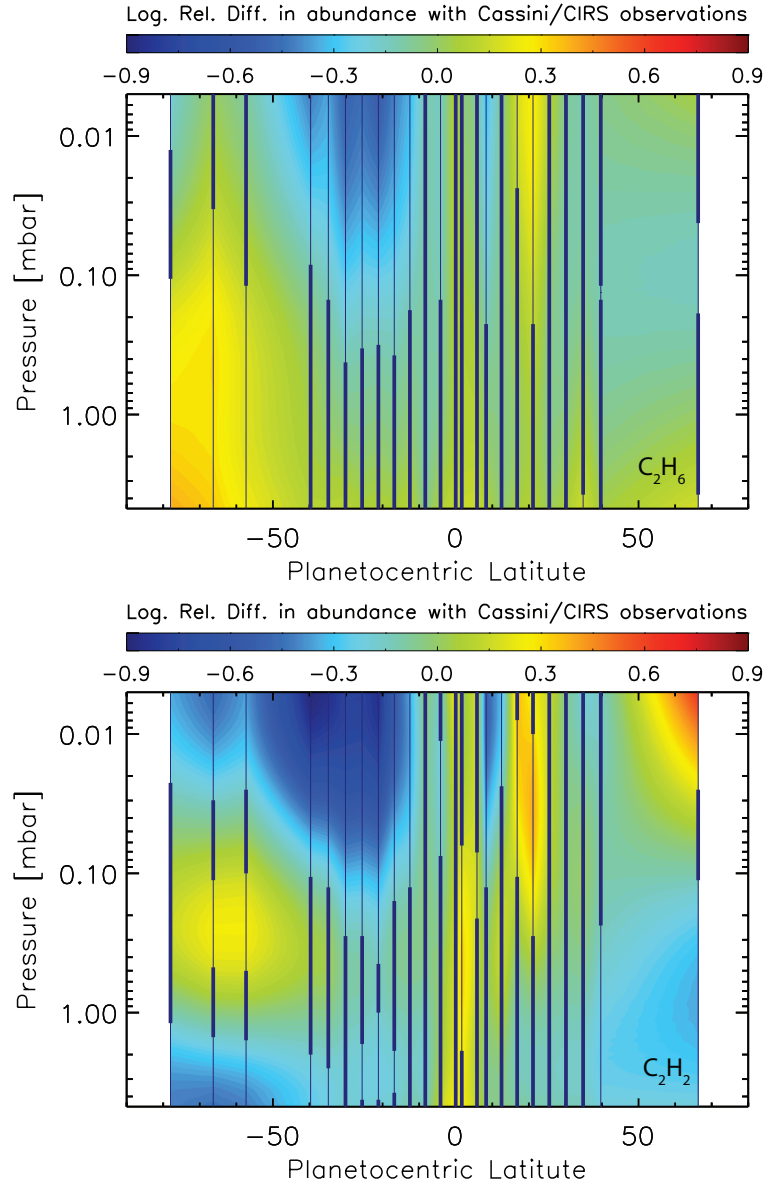
Figure 25: Same as Fig. (24) using the photochemical predictions that use (U) thermal field.
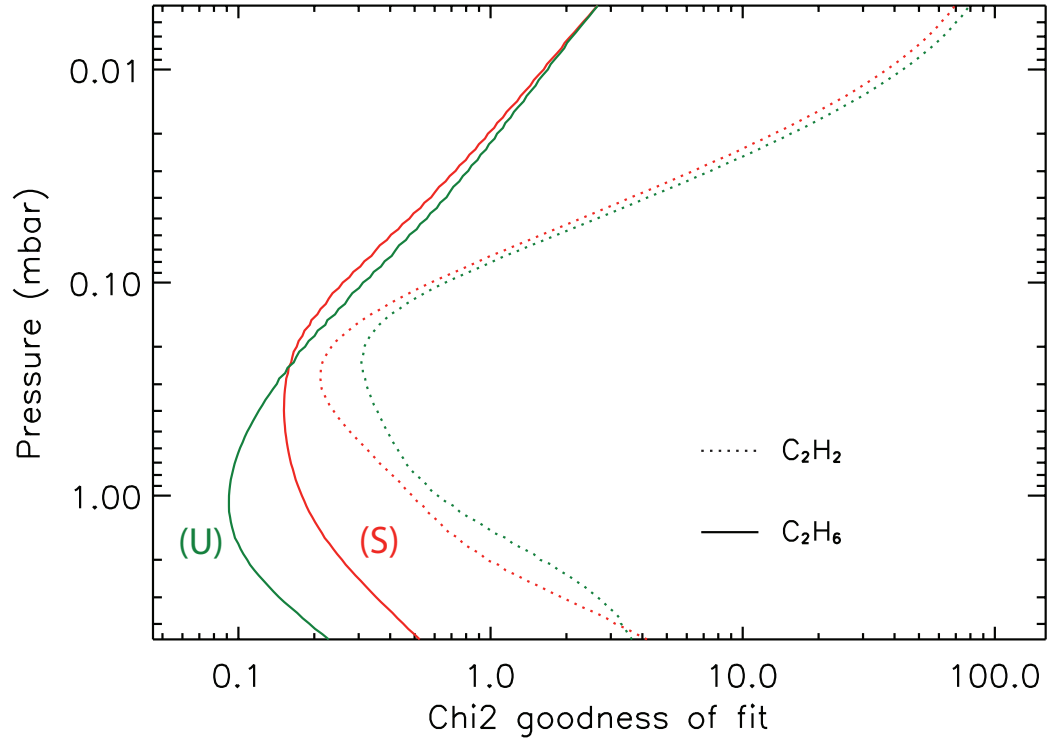
Figure 26: Evolution of the χ square goodness-of-fit factor for C_2H_2 (dotted lines) and C_2H_6 (dashed lines) over the sensitivity pressure ranges of the Cassini/CIRS limb observation mode. This factor is presented when using (S) and (U) thermal fields, denoted by the red and green lines respectively. This factor is summed for all observed latitudes.

5.4. Discussion

As noted above, it has been shown that both C_2H_6 and C_2H_2 were overpredicted at mid-southern latitudes and above $0.1\,\text{mbar}$, while C_2H_6 was underpredicted at high-southern latitudes and below $0.01\,\text{mbar}$ (recall Fig. 24). It can be pointed out that the eddy diffusion coefficient used in this work was possibly not the most optimal one. We remind the reader that the coefficient used here was chosen so that it provides a satisfactory fit of the CH_4 vertical profile in comparison to Voyager/UVS and Cassini/CIRS data (Smith et al., 1983; Dobrijevic et al., 2011).

However, when looking carefully at the southern mid latitudes in Figs. 23 and 24, where we overpredict the C_2H_6 abundance above $0.1\,\text{mbar}$ and underpredict its abundance below $1\,\text{mbar}$, a diffusion coefficient greater in the upper stratosphere (above $0.1\,\text{mbar}$) and smaller below that level might provide a better fit at these latitudes. We have performed a sensitivity study on that parameter by using several dozen different eddy diffusion coefficients. The seasonal model was run from the converged state with the nominal eddy diffusion profile presented in this work. From that point, the eddy diffusion profile was modified and several additional iterations over Saturn orbits were necessary for the system to converge, depending on the new eddy diffusion coefficient. Several different eddy diffusion coefficients provide a better fit of mid-latitudes in the southern hemisphere, but at the same time the good agreement in the northern hemisphere vanishes.

All along this study, we have assumed an eddy coefficient constant with latitudes. However, the sensitivity study on that free parameter has shown us that some latitudes that were not properly reproduced with an eddy diffusion coefficient based on globally averaged observations could be reproduced when adjusting this coefficient. In principle, it could therefore be possible to fit all the observed latitudes by finding the most adapted diffusion coefficient at each latitude. We have not explored this possibility more extensively since the meridional variability of that parameter has not yet been demonstrated with the observation of the latitudinal variability of CH_4 homopause.

Another likely possibility would be the existence of large scale meridional transport (diffusive and/or advective), as the associated atmospheric motions might be an important source of departure from the photochemical predictions (Moses and Greathouse, 2005; Guerlet et al., 2009, 2010; Friedson and Moses, 2012; Sinclair et al., 2013). However, it is difficult to assess the validity of this hypothesis without further numerical testing. Such work is defered to a later paper. The recommended methodology would be first to

retrieve the latitudinal variability of the CH_4 homopause in order to better constrain the latitudinal variability of the eddy diffusion coefficient before fitting the Cassini/CIRS observations with meridional transport.

Predictions of the existence of large-scale circulation have already been studied using numerical models. Conrath et al. (1990), using a 2D zonally averaged model, have predicted a summer-to-winter pole stratospheric circulation cell for Saturn at solstice with upwelling around the summer pole and downwelling around the winter pole. They also found a double circulation cell at equinox, with upwelling at equator and downwelling at both poles. However their calculations did not include aerosols heating which is known to impact the radiative budget in the atmosphere. Afterwards, West et al. (1992) included such heating for a Jovian-like planet and showed that circulation was altered above 100 mbar, with downwelling at equator and upwelling at the poles. We note that they have not presented the effect of aerosol heating on a Saturn-like planet at solstice. Recently, Friedson and Moses (2012) predicted a seasonally reversing circulation cell using a 3D GCM, with upwelling at the equator and downwelling at low latitudes in the winter hemisphere. The next step of this study is to evaluate whether these predicted circulation patterns are sufficient for our full 2D photochemical model to reproduce the Cassini data.

6. Summary and perspectives

We have developed a latitudinally and seasonally variable photochemical model for giant planets and we have adapted it first to Saturn. The model takes into account photochemistry, vertical mixing, Saturn's obliquity, and variation of seasonally dependent orbital parameters such as subsolar latitude, heliocentric distance and ring shadowing. Meridional transport (both advective and diffusive) as well as vertical advective transport have been coded in the model but have been switched off for the current study. The present model is therefore run as a sum of 1D seasonally variable models calculated at different latitudes. This is the first step toward a full-2D model as it is already coupled to a full-3D radiative transfer model. This first paper is dedicated to the study of the photochemical effects involved by a seasonally variable thermal field, which relies on predictions from a radiative climate model (Greathouse et al., 2008).

Seasonal variability of C_2H_2 and C_2H_6. - The seasonal variations of the C2-hydrocarbon mole fractions such as C_2H_2 (acetylene) and C_2H_6 (ethane)

are important at pressure levels lower than 0.1 mbar and at high latitudes. These compounds are known to act as the main stratospheric coolants (Yelle et al., 2001) and we therefore have emphasized them in this work on their seasonal variabilities. These hydrocarbons are produced by chemical reactions involving radicals which strongly depend on insolation. Including the ring shadowing effect generally results in lowering the mole fraction of hydrocarbons at latitudes that are under the shadow of the rings. The decrease in the mole fraction of these compounds caused by the rings is more important for C_2H_2 than for C_2H_6. This decrease tends to vanish at higher-pressure levels.

Accounting for a seasonally variable thermal field. - We found that including a seasonally variable thermal field mainly impacts the seasonal evolution of the hydrocarbon mole fractions in two ways. First, the modification of the thermal field amplitude will affect the position of the methane homopause and will impact consequently the integrated production rates of radicals above the pressure level of 10^{-4} mbar. Then, accounting for a seasonally variable thermal field will affect the diffusion of these produced hydrocarbons through the contraction and dilatation of the atmospheric columns. This will compress the vertical distribution of the atmospheric compounds and will therefore increase the diffusion of these compounds to higher pressure levels. Because the former effect is correlated with the seasonal variation of temperature of the atmospheric column, it is therefore increased with increasing latitude, i.e. where the seasonal thermal gradients are strong. At 10^{-4} mbar, C_2H_2 and C_2H_6 seasonal abundance gradients are generally enhanced. At this pressure level and during the summer season, C_2H_6 shows a positive equator-to-summer pole (North or South) gradient. At 10^{-2} mbar, the seasonal abundance gradients are also increased: the abundance of C_2H_6 and C_2H_2 are respectively decreased by a factor of 2.2 and 1.7 at a latitude of $80°$ during winter, with respect to the (U) study case. We do not reach the same conclusions than Moses and Greathouse (2005) about the thermal sensitivity of the photochemical model. While our (U) study case is similar to their approach, our (S) study case is, on the other hand, different in a way that the compounds mole fractions are assumed to follow the atmospheric contraction/dilatation in the pressure space with changing thermodynamic conditions. This consequently affects the downward diffusion of the seasonally produced photochemical by-products.

Comparison with Cassini/CIRS data. - The Cassini spacecraft has now provided an important amount of data that includes good spatial and tempo-

ral coverage (Sinclair et al., 2013) as well as good vertical sensitivity (Guerlet et al., 2009, 2010). Our model reproduces reasonnably well the meridional distributions of C_2H_2 and C_2H_6 up to mid-latitudes, even without meridional circulation. However, the overall increase of C_2H_6 from the south pole towards the north pole at $L_s=320°$ is not reproduced. An interesting feature has been noted: our model tends to underpredict C_2H_6 abundance from 40°S to South pole at pressure levels ranging from 5 mbar to 0.1 mbar and overpredict its abundance at latitude ranging from 10°S to 40°S at pressure ranging from 5×10^{-3} to 0.1 mbar. These results are consistent with previous findings of Guerlet et al. (2009, 2010) and Sinclair et al. (2013). This interesting feature is also observed for C_2H_2, although in a less pronounced way. The forthcoming step is to turn on the meridional transport to evaluate if it can help better fit to the Cassini data.

Coupling radiative climate model and photochemical model Accounting for these results may have important implications for radiative climate models and GCMs because the predicted temperatures from these models are very sensitive to the amount of these coolants (Greathouse et al., 2008). From 0.1 to 10^{-4} mbar, where their seasonal variability is important, the increase in the amount of these coolants during the summer season will likely counteract the increase in the atmospheric heating caused by the increase in the solar insolation at high-latitudes. Depending on the relative magnitudes of the photochemical timescale over the thermal inertia timescale, the peak in the predicted temperatures at high-latitudes could happen earlier around the summer solstice than previously predicted using a radiative climate model which uses time-independant abundances of atmospheric coolants. The predicted temperatures are therefore expected to start decreasing earlier after summer solstice than what would be predicted with a model that held the amount of these atmospheric coolants constant over time. Moreover, the effect on the lower-stratosphere could be also interesting, as we showed that accounting for the seasonal evolution of the thermal field impacts the phase-lag and the seasonal variability in this region.

7. Acknowledgement

References

Agúndez, M., Parmentier, V., Venot, O., Hersant, F., Selsis, F., 2014. Pseudo 2D chemical model of hot-Jupiter atmospheres: application to HD 209458b and HD 189733b. Astron. Astrophys. 564, A73.

Banfield, D., Gierasch, P. J., Squyres, S. W., Nicholson, P. D., Conrath, B. J., Matthews, K., Jun. 1996. 2 μm Spectrophotometry of Jovian Stratospheric Aerosols—Scattering Opacities, Vertical Distributions, and Wind Speeds. Icarus 121, 389–410.

Bézard, B., 1986. Variations saisonnières de la structure thermique et composition chimique de jupiter, saturne et uranus. Ph.D. thesis.

Bézard, B., Gautier, D., 1985. A seasonal climate model of the atmospheres of the giant planets at the Voyager encounter time. I - Saturn's stratosphere. Icarus 61, 296–310.

Bézard, B., Gautier, D., Conrath, B., 1984. A seasonal model of the Saturnian upper troposphere Comparison with Voyager infrared measurements. Icarus 60, 274–288.

Brillet, J., Parisot, J. P., Dobrijevic, M., Leflochmoen, E., Toublanc, D., 1996. A three-dimensional simulation of transmitted light through planetary atmospheres using Monte-Carlo methods. Adv. Space Res. 17, 223–226.

Brinkman, A. W., McGregor, J., 1979. The effect of the ring system of the solar radiation reaching the top of Saturn's atmosphere - Direct radiation. Icarus 38, 479–482.

Cavalié, T., Dobrijevic, M., Fletcher, L. N., Loison, J. C., Hickson, K. M., Hue, V., Hartogh, P., 2015. The photochemical response to the variation of temperature in Saturn's 2011-2012 stratospheric vortex. Astron. Astrophys., revised.

Cess, R. D., Caldwell, J., 1979. A Saturnian stratospheric seasonal climate model. Icarus 38, 349–357.

Colwell, J. E., Esposito, L. W., Jerousek, R. G., Sremčević, M., Pettis, D., Bradley, E. T., 2010. Cassini UVIS Stellar Occultation Observations of Saturn's Rings. Astron. J. 140, 1569–1578.

Conrath, B. J., Gautier, D., 2000. Saturn Helium Abundance: A Reanalysis of Voyager Measurements. Icarus 144, 124–134.

Conrath, B. J., Gierasch, P. J., Leroy, S. S., 1990. Temperature and circulation in the stratosphere of the outer planets. Icarus 83, 255–281.

Conrath, B. J., Pirraglia, J. A., Feb. 1983. Thermal structure of Saturn from Voyager infrared measurements - Implications for atmospheric dynamics. Icarus53, 286–292.

Courtin, R., Gautier, D., Marten, A., Bezard, B., Hanel, R., Dec. 1984. The composition of Saturn's atmosphere at northern temperate latitudes from Voyager IRIS spectra - NH3, PH3, C2H2, C2H6, CH3D, CH4, and the Saturnian D/H isotopic ratio. ApJ287, 899–916.

Dobrijevic, M., Cavalié, T., Billebaud, F., 2011. A methodology to construct a reduced chemical scheme for 2D-3D photochemical models: Application to Saturn. Icarus 214, 275–285.

Dobrijevic, M., Cavalié, T., Hébrard, E., Billebaud, F., Hersant, F., Selsis, F., 2010a. Key reactions in the photochemistry of hydrocarbons in Neptune's stratosphere. Planet. Space Sci. 58, 1555–1566.

Dobrijevic, M., Hébrard, E., Loison, J. C., Hickson, K. M., 2014. Coupling of oxygen, nitrogen, and hydrocarbon species in the photochemistry of Titan's atmosphere. Icarus 228, 324–346.

Dobrijevic, M., Hébrard, E., Plessis, S., Carrasco, N., Pernot, P., Bruno-Claeys, M., 2010b. Comparison of methods for the determination of key

reactions in chemical systems: Application to Titan's atmosphere. Adv. Space Res. 45, 77–91.

Dobrijevic, M., Ollivier, J. L., Billebaud, F., Brillet, J., Parisot, J. P., 2003. Effect of chemical kinetic uncertainties on photochemical modeling results: Application to Saturn's atmosphere. Astron. Astrophys. 398, 335–344.

Dobrijevic, M., Parisot, J. P., 1998. Effect of chemical kinetics uncertainties on hydrocarbon production in the stratosphere of Neptune. Planet. Space Sci. 46, 491–505.

Dowling, T. E., Bradley, M. E., Colón, E., Kramer, J., LeBeau, R. P., Lee, G. C. H., Mattox, T. I., Morales-Juberías, R., Palotai, C. J., Parimi, V. K., Showman, A. P., 2006. The EPIC atmospheric model with an isentropic/terrain-following hybrid vertical coordinate. Icarus 182, 259–273.

Dowling, T. E., Greathouse, T. K., Sussman, M. G., Chanover, N. J., 2010. New Radiative Transfer Capability in the EPIC Atmospheric Model with Application to Saturn and Uranus. In: AAS/Division for Planetary Sciences Meeting Abstracts #42. Vol. 42 of Bulletin of the American Astronomical Society. p. 1021.

Edgington, S. G., Atreya, S. K., Wilson, E. H., West, R. A., Baines, K. H., Bjoraker, G. L., Fletcher, L. N., Momary, T., 2012. Photochemistry in Saturn's Ring Shadowed Atmosphere: Production Rates of Key Atmospheric Molecules and Preliminary Analysis of Observations. AGU Fall Meeting Abstracts, B1946.

Fischer, G., Kurth, W., Gurnett, D., Zarka, P., Dyudina, U., Ingersoll, A., Ewald, S., Porco, C., Wesley, A., Go, C., et al., 2011. A giant thunderstorm on saturn. Nature 475 (7354), 75–77.

Flasar, F. M., Achterberg, R. K., Conrath, B. J., Pearl, J. C., Bjoraker, G. L., Jennings, D. E., Romani, P. N., Simon-Miller, A. A., Kunde, V. G., Nixon, C. A., Bézard, B., Orton, G. S., Spilker, L. J., Spencer, J. R., Irwin, P. G. J., Teanby, N. A., Owen, T. C., Brasunas, J., Segura, M. E., Carlson, R. C., Mamoutkine, A., Gierasch, P. J., Schinder, P. J., Showalter, M. R., Ferrari, C., Barucci, A., Courtin, R., Coustenis, A., Fouchet, T., Gautier, D., Lellouch, E., Marten, A., Prangé, R., Strobel, D. F., Calcutt, S. B.,

Read, P. L., Taylor, F. W., Bowles, N., Samuelson, R. E., Abbas, M. M., Raulin, F., Ade, P., Edgington, S., Pilorz, S., Wallis, B., Wishnow, E. H., 2005. Temperatures, Winds, and Composition in the Saturnian System. Science 307, 1247–1251.

Flasar, F. M., Kunde, V. G., Achterberg, R. K., Conrath, B. J., Simon-Miller, A. A., Nixon, C. A., Gierasch, P. J., Romani, P. N., Bézard, B., Irwin, P., Bjoraker, G. L., Brasunas, J. C., Jennings, D. E., Pearl, J. C., Smith, M. D., Orton, G. S., Spilker, L. J., Carlson, R., Calcutt, S. B., Read, P. L., Taylor, F. W., Parrish, P., Barucci, A., Courtin, R., Coustenis, A., Gautier, D., Lellouch, E., Marten, A., Prangé, R., Biraud, Y., Fouchet, T., Ferrari, C., Owen, T. C., Abbas, M. M., Samuelson, R. E., Raulin, F., Ade, P., Césarsky, C. J., Grossman, K. U., Coradini, A., 2004. An intense stratospheric jet on Jupiter. Nature 427, 132–135.

Fletcher, L. N., Achterberg, R. K., Greathouse, T. K., Orton, G. S., Conrath, B. J., Simon-Miller, A. A., Teanby, N., Guerlet, S., Irwin, P. G. J., Flasar, F. M., 2010. Seasonal change on Saturn from Cassini/CIRS observations, 2004-2009. Icarus 208, 337–352.

Fletcher, L. N., Hesman, B. E., Achterberg, R. K., Irwin, P. G. J., Bjoraker, G., Gorius, N., Hurley, J., Sinclair, J., Orton, G. S., Legarreta, J., García-Melendo, E., Sánchez-Lavega, A., Read, P. L., Simon-Miller, A. A., Flasar, F. M., 2012. The origin and evolution of Saturn's 2011-2012 stratospheric vortex. Icarus 221, 560–586.

Fletcher, L. N., Hesman, B. E., Irwin, P. G., Baines, K. H., Momary, T. W., Sanchez-Lavega, A., Flasar, F. M., Read, P. L., Orton, G. S., Simon-Miller, A., et al., 2011. Thermal structure and dynamics of saturns northern springtime disturbance. Science 332 (6036), 1413–1417.

Fletcher, L. N., Irwin, P. G. J., Teanby, N. A., Orton, G. S., Parrish, P. D., de Kok, R., Howett, C., Calcutt, S. B., Bowles, N., Taylor, F. W., 2007. Characterising Saturn's vertical temperature structure from Cassini/CIRS. Icarus 189, 457–478.

Fletcher, L. N., Orton, G. S., Teanby, N. A., Irwin, P. G. J., Bjoraker, G. L., 2009. Methane and its isotopologues on Saturn from Cassini/CIRS observations. Icarus 199, 351–367.

Fouchet, T., Guerlet, S., Strobel, D. F., Simon-Miller, A. A., Bézard, B., Flasar, F. M., 2008. An equatorial oscillation in Saturn's middle atmosphere. Nature 453, 200–202.

Fouchet, T., Moses, J. I., Conrath, B. J., 2009. Saturn: Composition and Chemistry. p. 83.

Friedson, A. J., Moses, J. I., 2012. General circulation and transport in Saturn's upper troposphere and stratosphere. Icarus 218, 861–875.

Fuller, E. N., Ensley, K., Giddings, J. C., 1969. Diffusion of halogenated hydrocarbons in helium. the effect of structure on collision cross sections. The Journal of Physical Chemistry 73 (11), 3679–3685.

Fuller, E. N., Schettler, P. D., Giddings, J. C., 1966. New method for prediction of binary gas-phase diffusion coefficients. Industrial and Engineering Chemistry 58 (5), 18–27.

Gezari, D. Y., Mumma, M. J., Espenak, F., Deming, D., Bjoraker, G., Woods, L., Folz, W., 1989. New features in Saturn's atmosphere revealed by high-resolution thermal infrared images. Nature 342, 777–780.

Gillett, F. C., Orton, G. S., Jan. 1975. Center-to-limb observations of Saturn in the thermal infrared. ApJ195, L47–L49.

Godunov, S., 1959. A Difference Scheme for Numerical Solution of Discontinuous solution of Hydrodynamic Equations. Math. Sbornik 47, 271–306.

Greathouse, T. K., Lacy, J. H., Bézard, B., Moses, J. I., Griffith, C. A., Richter, M. J., 2005. Meridional variations of temperature, C_2H_2 and C_2H_6 abundances in Saturn's stratosphere at southern summer solstice. Icarus 177, 18–31.

Greathouse, T. K., Strong, S., Moses, J., Orton, G., Fletcher, L., Dowling, T., 2008. A General Radiative Seasonal Climate Model Applied to Saturn, Uranus, and Neptune. AGU Fall Meeting Abstracts, B6.

Guerlet, S., Fouchet, T., Bézard, B., Flasar, F. M., Simon-Miller, A. A., 2011. Evolution of the equatorial oscillation in Saturn's stratosphere between 2005 and 2010 from Cassini/CIRS limb data analysis. Geophys. Res. Lett. 38, 9201.

Guerlet, S., Fouchet, T., Bézard, B., Moses, J. I., Fletcher, L. N., Simon-Miller, A. A., Michael Flasar, F., 2010. Meridional distribution of CH_3C_2H and C_4H_2 in Saturn's stratosphere from CIRS/Cassini limb and nadir observations. Icarus 209, 682–695.

Guerlet, S., Fouchet, T., Bézard, B., Simon-Miller, A. A., Michael Flasar, F., 2009. Vertical and meridional distribution of ethane, acetylene and propane in Saturn's stratosphere from CIRS/Cassini limb observations. Icarus 203, 214–232.

Guerlet, S., Spiga, A., Sylvestre, M., Indurain, M., Fouchet, T., Leconte, J., Millour, E., Wordsworth, R., Capderou, M., Bzard, B., Forget, F., 2014. Global climate modeling of saturns atmosphere. part i: Evaluation of the radiative transfer model. Icarus 238 (0), 110 – 124.

Guillot, T., 2005. The Interiors of Giant Planets: Models and Outstanding Questions. Annual Review of Earth and Planetary Sciences 33, 493–530.

Hanel, R., Conrath, B., Flasar, F. M., Kunde, V., Maguire, W., Pearl, J. C., Pirraglia, J., Samuelson, R., Cruikshank, D. P., Gautier, D., Gierasch, P. J., Horn, L., Ponnamperuma, C., 1982. Infrared observations of the Saturnian system from Voyager 2. Science 215, 544–548.

Hanel, R., Conrath, B., Flasar, F. M., Kunde, V., Maguire, W., Pearl, J. C., Pirraglia, J., Samuelson, R., Herath, L., Allison, M., Cruikshank, D. P., Gautier, D., Gierasch, P. J., Horn, L., Koppany, R., Ponnamperuma, C., 1981. Infrared observations of the Saturnian system from Voyager 1. Science 212, 192–200.

Hartogh, P., Lellouch, E., Crovisier, J., Banaszkiewicz, M., Bensch, F., Bergin, E. A., Billebaud, F., Biver, N., Blake, G. A., Blecka, M. I., Blommaert, J., Bockelée-Morvan, D., Cavalié, T., Cernicharo, J., Courtin, R., Davis, G., Decin, L., Encrenaz, P., Encrenaz, T., González, A., de Graauw, T., Hutsemékers, D., Jarchow, C., Jehin, E., Kidger, M., Küppers, M., de Lange, A., Lara, L.-M., Lis, D. C., Lorente, R., Manfroid, J., Medvedev, A. S., Moreno, R., Naylor, D. A., Orton, G., Portyankina, G., Rengel, M., Sagawa, H., Sánchez-Portal, M., Schieder, R., Sidher, S., Stam, D., Swinyard, B., Szutowicz, S., Thomas, N., Thornhill, G., Vandenbussche,

B., Verdugo, E., Waelkens, C., Walker, H., 2009. Water and related chemistry in the solar system. A guaranteed time key programme for Herschel. Planet. Space Sci. 57, 1596–1606.

Hartogh, P., Lellouch, E., Moreno, R., Bockelée-Morvan, D., Biver, N., Cassidy, T., Rengel, M., Jarchow, C., Cavalié, T., Crovisier, J., Helmich, F. P., Kidger, M., 2011. Direct detection of the Enceladus water torus with Herschel. Astron. Astrophys. 532, L2.

Hébrard, E., Dobrijevic, M., Loison, J. C., Bergeat, A., Hickson, K. M., Caralp, F., 2013. Photochemistry of C_3H_p hydrocarbons in Titan's stratosphere revisited. Astron. Astrophys. 552, A132.

Hesman, B. E., Jennings, D. E., Sada, P. V., Bjoraker, G. L., Achterberg, R. K., Simon-Miller, A. A., Anderson, C. M., Boyle, R. J., Nixon, C. A., Fletcher, L. N., McCabe, G. H., 2009. Saturn's latitudinal C_2H_2 and C_2H_6 abundance profiles from Cassini/CIRS and ground-based observations. Icarus 202, 249–259.

Howett, C. J. A., Irwin, P. G. J., Teanby, N. A., Simon-Miller, A., Calcutt, S. B., Fletcher, L. N., de Kok, R., 2007. Meridional variations in stratospheric acetylene and ethane in the southern hemisphere of the saturnian atmosphere as determined from Cassini/CIRS measurements. Icarus 190, 556–572.

Ingersoll, A. P., Pollard, D., Oct. 1982. Motion in the interiors and atmospheres of Jupiter and Saturn - Scale analysis, anelastic equations, barotropic stability criterion. Icarus52, 62–80.

Irwin, P., 2006. Giant Planets of Our Solar System: An Introduction. Springer Praxis Books / Astronomy and Planetary Sciences Series. Springer.

Li, L., Conrath, B. J., Gierasch, P. J., Achterberg, R. K., Nixon, C. A., Simon-Miller, A. A., Flasar, F. M., Banfield, D., Baines, K. H., West, R. A., Ingersoll, A. P., Vasavada, A. R., Del Genio, A. D., Porco, C. C., Mamoutkine, A. A., Segura, M. E., Bjoraker, G. L., Orton, G. S., Fletcher, L. N., Irwin, P. G. J., Read, P. L., Nov. 2010. Saturn's emitted power. Journal of Geophysical Research (Planets) 115, 11002.

Liang, M.-C., Shia, R.-L., Lee, A. Y.-T., Allen, M., Friedson, A. J., Yung, Y. L., 2005. Meridional Transport in the Stratosphere of Jupiter. Astrophys. J.l 635, L177–L180.

Lindal, G. F., Sweetnam, D. N., Eshleman, V. R., Jun. 1985. The atmosphere of Saturn - an analysis of the Voyager radio occultation measurements. AJ90, 1136–1146.

Lindzen, R., 1971. Tides and gravity waves in the upper atmosphere(internal gravity waves and tidal oscillations excitation mechanism in upper atmosphere). Mesospheric Models and Related Experiments, 122130.

Lindzen, R. S., 1981. Turbulence and stress owing to gravity wave and tidal breakdown. Journal of Geophysical Research: Oceans (1978–2012) 86 (C10), 9707–9714.

Loison, J. C., Hébrard, E., Dobrijevic, M., Hickson, K. M., Caralp, F., Hue, V., Gronoff, G., Venot, O., Benilan, Y., 2014. The neutral photochemistry of nitriles, amines and imines in the atmosphere of titan. Icarus, in press.

Medvedev, A. S., Sethunadh, J., Hartogh, P., 2013. From cold to warm gas giants: A three-dimensional atmospheric general circulation modeling. Icarus 225, 228–235.

Moreno, R., Marten, A., Matthews, H. E., Biraud, Y., 2003. Long-term evolution of CO, CS and HCN in Jupiter after the impacts of comet Shoemaker-Levy 9. Planet. Space Sci. 51, 591–611.

Moses, J. I., Bézard, B., Lellouch, E., Gladstone, G. R., Feuchtgruber, H., Allen, M., 2000a. Photochemistry of Saturn's Atmosphere. I. Hydrocarbon Chemistry and Comparisons with ISO Observations. Icarus 143, 244–298.

Moses, J. I., Fouchet, T., Bézard, B., Gladstone, G. R., Lellouch, E., Feuchtgruber, H., 2005. Photochemistry and diffusion in Jupiter's stratosphere: Constraints from ISO observations and comparisons with other giant planets. J. Geophys. Res. 110, 8001.

Moses, J. I., Greathouse, T. K., 2005. Latitudinal and seasonal models of stratospheric photochemistry on Saturn: Comparison with infrared data from IRTF/TEXES. Journal of Geophysical Research (Planets) 110, 9007.

Moses, J. I., Lellouch, E., Bézard, B., Gladstone, G. R., Feuchtgruber, H., Allen, M., 2000b. Photochemistry of Saturn's Atmosphere. II. Effects of an Influx of External Oxygen. Icarus 145, 166–202.

Moses, J. I., Liang, M.-C., Yung, Y. L., Shia, R.-L., 2007. Meridional Distribution of Hydrocarbons on Saturn: Implications for Stratospheric Transport. In: Planetary Atmospheres. pp. 85–86.

Ollivier, J. L., Billebaud, F., Drossart, P., Dobrijévic, M., Roos-Serote, M., August-Bernex, T., Vauglin, I., 2000a. Seasonal effects in the thermal structure of Saturn's stratosphere from infrared imaging at 10 microns. Astron. Astrophys. 356, 347–356.

Ollivier, J. L., Dobrijévic, M., Parisot, J. P., 2000b. New photochemical model of Saturn's atmosphere. Planet. Space Sci. 48, 699–716.

Orton, G. S., Yanamandra-Fisher, P. A., Fisher, B. M., Friedson, A. J., Parrish, P. D., Nelson, J. F., Bauermeister, A. S., Fletcher, L., Gezari, D. Y., Varosi, F., Tokunaga, A. T., Caldwell, J., Baines, K. H., Hora, J. L., Ressler, M. E., Fujiyoshi, T., Fuse, T., Hagopian, H., Martin, T. Z., Bergstralh, J. T., Howett, C., Hoffmann, W. F., Deutsch, L. K., van Cleve, J. E., Noe, E., Adams, J. D., Kassis, M., Tollestrup, E., 2008. Semi-annual oscillations in Saturn's low-latitude stratospheric temperatures. Nature 453, 196–199.

Pirraglia, J. A., Conrath, B. J., Allison, M. D., Gierasch, P. J., Aug. 1981. Thermal structure and dynamics of Saturn and Jupiter. Nature292, 677–679.

Rieke, G. H., Sep. 1975. The thermal radiation of Saturn and its rings. Icarus26, 37–44.

Romani, P. N., Atreya, S. K., 1988. Methane photochemistry and methane production on Neptune. Icarus 74, 424–445.

Sánchez-Lavega, A., del Río-Gaztelurrutia, T., Hueso, R., Gómez-Forrellad, J. M., Sanz-Requena, J. F., Legarreta, J., García-Melendo, E., Colas, F., Lecacheux, J., Fletcher, L. N., Barrado y Navascués, D., Parker, D., International Outer Planet Watch Team, Akutsu, T., Barry, T., Beltran, J., Buda, S., Combs, B., Carvalho, F., Casquinha, P., Delcroix, M.,

Ghomizadeh, S., Go, C., Hotershall, J., Ikemura, T., Jolly, G., Kazemoto, A., Kumamori, T., Lecompte, M., Maxson, P., Melillo, F. J., Milika, D. P., Morales, E., Peach, D., Phillips, J., Poupeau, J. J., Sussenbach, J., Walker, G., Walker, S., Tranter, T., Wesley, A., Wilson, T., Yunoki, K., 2011. Deep winds beneath Saturn's upper clouds from a seasonal long-lived planetary-scale storm. Nature 475, 71–74.

Simon-Miller, A. A., Bjoraker, G. L., Jennings, D. E., Achterberg, R. K., Conrath, B. J., Nixon, C. A., Cassini CIRS Team, 2005. Cassini CIRS Measurements of Benzene, Propane and Carbon Dioxide on Saturn. In: AAS/Division for Planetary Sciences Meeting Abstracts #37. Vol. 37 of Bulletin of the American Astronomical Society. p. 682.

Sinclair, J. A., Irwin, P. G. J., Fletcher, L. N., Greathouse, T., Guerlet, S., Hurley, J., Merlet, C., May 2014. From Voyager-IRIS to Cassini-CIRS: Interannual variability in Saturn's stratosphere? Icarus 233, 281–292.

Sinclair, J. A., Irwin, P. G. J., Fletcher, L. N., Moses, J. I., Greathouse, T. K., Friedson, A. J., Hesman, B., Hurley, J., Merlet, C., 2013. Seasonal variations of temperature, acetylene and ethane in Saturn's atmosphere from 2005 to 2010, as observed by Cassini-CIRS. Icarus 225, 257–271.

Smith, B. A., Soderblom, L., Batson, R. M., Bridges, P. M., Inge, J. L., Masursky, H., Shoemaker, E., Beebe, R. F., Boyce, J., Briggs, G., Bunker, A., Collins, S. A., Hansen, C., Johnson, T. V., Mitchell, J. L., Terrile, R. J., Cook, A. F., Cuzzi, J. N., Pollack, J. B., Danielson, G. E., Ingersoll, A. P., Davies, M. E., Hunt, G. E., Morrison, D., Owen, T., Sagan, C., Veverka, J., Strom, R., Suomi, V. E., Jan. 1982. A new look at the Saturn system - The Voyager 2 images. Science 215, 504–537.

Smith, G. R., Shemansky, D. E., Holberg, J. B., Broadfoot, A. L., Sandel, B. R., McConnell, J. C., 1983. Saturn's upper atmosphere from the Voyager 2 EUV solar and stellar occultations. J. Geophys. Res. 88, 8667–8678.

Tokunaga, A. T., Caldwell, J., Gillett, F. C., Nolt, I. G., 1978. Spatially resolved infrared observations of Saturn. II - The temperature enhancement at the South Pole of Saturn. Icarus 36, 216–222.

West, R. A., Friedson, A. J., Appleby, J. F., 1992. Jovian large-scale stratospheric circulation. Icarus 100, 245–259.

Yelle, R. V., Griffith, C. A., Young, L. A., 2001. Structure of the Jovian Stratosphere at the Galileo Probe Entry Site. Icarus 152, 331–346.

Zhang, X., Shia, R.-L., Yung, Y. L., 2013. Jovian Stratosphere as a Chemical Transport System: Benchmark Analytical Solutions. Astrophys. J. 767, 172.